

The Pennsylvania State University

The Graduate School

Eberly College of Science

**NMR, X-RAY, AND INFRARED CHARACTERIZATION OF DYNAMICS  
AND STRUCTURE IN IONIC LIQUIDS AND SOLIDS**

A Thesis in

Chemistry

by

Caleb Uitvlugt

© 2019 Caleb Uitvlugt

Submitted in Partial Fulfillment

of the Requirements

for the Degree of

Master of Science

May 2019

The thesis of Caleb Uitvlugt was reviewed and approved\* by the following:

Mark Maroncelli

Distinguished Professor of Chemistry

Thesis Adviser

Scott A. Showalter

Associate Professor of Chemistry, Biochemistry, & Molecular Biology

Graduate Program Chair

Alexey Silakov

Assistant Professor of Chemistry

Michael Hickner

Professor of Materials Science & Engineering, Chemical Engineering

Philip Bevilacqua

Distinguished Professor of Chemistry, Biochemistry, & Molecular Biology

\*Signatures are on file in the Graduate School.

## Abstract

In this work, the structure and dynamics of ionic liquid systems were investigated using nuclear magnetic resonance (NMR) spectroscopy, differential scanning calorimetry (DSC), X-ray scattering, and infrared (IR) spectroscopy. Two studies of the ionic liquid 1-butyl-3-methylimidazolium tetrafluoroborate ( $[\text{Im}_{41}][\text{BF}_4]$ ) were performed. These are described in Chapter 1. One entailed studying the rotation of dimethylbenzene (DMBz) analogues and the other rotation and translational diffusion in mixtures of  $[\text{Im}_{41}][\text{BF}_4]$  with the polar aprotic solvent acetonitrile (ACN). A third study was conducted of the solid form of the ionic liquid trimethyldecylammonium bis(perfluoroethylsulfonyl)imide ( $[\text{N}_{10,111}][\text{beti}]$ ) or DTAB.

The first set of rotational diffusion studies analyzed solutions of 1,4-dimethylbenzene- $\text{d}_{10}$  (DMBz), 1,4-dimethylpyridinium- $\text{d}_7$  hexafluorophosphate (DMPy), and p-tolunitrile- $\text{d}_7$  (CMBz) in  $[\text{Im}_{41}][\text{BF}_4]$ . These measurements, combined with molecular dynamics (MD) simulations performed by Chris Rumble, investigated the effects of molecular size, shape, and electrostatics on rotational dynamics in ionic liquids. For the second project,  $T_1$  relaxation times were measured in a set of mixtures ranging from neat  $[\text{Im}_{41}][\text{BF}_4]$  to neat ACN with benzene as a solute.  $T_1$  relaxation measurements were taken of  $[\text{Im}_{41}][\text{BF}_4]$ , ACN, and benzene to investigate the rotational dynamics of simple solutes as well as the solvent ions and the mixture was used to ask if there are fundamental differences. The NMR measurements gave the average rotation times of the  $[\text{Im}_{41}][\text{BF}_4]$  + ACN mixture, which were used by Brian Conway as a point of comparison for MD simulations.

The third study examines the solid phase of the ionic compound  $[\text{N}_{10,111}][\text{beti}]$  which forms a unique optically clear solid near room temperature. Preliminary X-ray diffraction (XRD) and  $^{13}\text{C}$  nuclear magnetic resonance (NMR) measurements indicated a superposition of order and amorphous structure in the solid phase. Subsequent DSC, X-ray scattering,  $^2\text{H}$  NMR, and infrared

spectroscopy data are used to attempt to assign the solid phase of DTAB to three possible frameworks: plastic crystal, glacial state, and Frank-Kasper phases.

# Table of Contents

List of Figures .....	vii
List of Tables .....	ix
Ionic Liquid Nomenclature .....	x
<b>Chapter 1. Rotation in Ionic Liquids .....</b>	<b>1</b>
1.1. Introduction .....	1
1.2. Solute Rotation in Ionic Liquids .....	2
1.3. Solute Dynamics in an Ionic Liquid.....	4
A. Experimental.....	4
B. Results and Discussion .....	5
1.4. Solute and Solvent Dynamics in an IL and Acetonitrile Mixture .....	6
A. Introduction .....	6
B. Experimental.....	6
C. Results and Discussion .....	7
<b>Chapter 2. [N<sub>10,111</sub>][beti], a Distinctive Ionic Solid .....</b>	<b>11</b>
2.1. Introduction .....	11
A. Preliminary NMR Data.....	11
B. Preliminary X-ray Data.....	12
2.2. Types of Solids.....	14
A. Plastic Crystals .....	14
B. Glacial States .....	17
C. Frank-Kasper Phases.....	18
2.3. Differential Scanning Calorimetry .....	20
A. Introduction .....	20
B. Experimental.....	21

C. Results.....	21
2.4. X-ray Scattering .....	24
A. Introduction .....	24
B. Results.....	24
C. Time Evolution of DTAB.....	27
2.5. $^2\text{H}$ NMR.....	30
A. Introduction .....	30
B. Results.....	31
C. Discussion.....	33
2.6. Infrared Spectroscopy .....	35
A. Introduction .....	35
B. Results.....	36
2.7. Discussion of the Nature of the DTAB Solid .....	38
A. Is the DTAB Solid a Plastic Crystal? .....	38
B. Is the DTAB Solid a Glacial State? .....	39
C. Is the DTAB Solid Forming Frank-Kasper Phases?.....	40
2.8. Conclusion.....	42
<b>Chapter 3. Summary and Conclusions .....</b>	<b>43</b>
Appendix: NMR Calibration.....	45
References .....	52

## List of Figures

Figure 1.1. $^2\text{H}$ NMR probe molecules .....	4
Figure 1.2. Rotation times as a function of temperature for probe molecules.....	5
Figure 1.3. Deuterated $[\text{Im}_{41}][\text{BF}_4]$ .....	6
Figure 1.4. $T_1$ times as a function of viscosity in $[\text{Im}_{41}][\text{BF}_4]/\text{ACN}$ mixtures .....	7
Figure 1.5. Simple pulsed field gradient NMR pulse sequence.....	9
Figure 1.6. Comparison of Simulated and Experimental Diffusion Coefficients.....	10
Figure 2.1. $[\text{N}_{10,111}][\text{Tf}_2\text{N}]$ and $[\text{N}_{10,111}][\text{beti}]$ structures.....	11
Figure 2.2. $^{13}\text{C}$ spectra of $[\text{N}_{10,111}][\text{beti}]$ at 20 °C and 50 °C .....	11
Figure 2.3. X-ray diffraction spectra of $[\text{N}_{10,111}][\text{Tf}_2\text{N}]$ and $[\text{N}_{10,111}][\text{beti}]$ .....	12
Figure 2.4. NMR linewidths for $^1\text{H}$ and $^{19}\text{F}$ of $[\text{P}_{1224}][\text{PF}_6]$ .....	16
Figure 2.5. Low-frequency Raman spectra of triphenyl phosphite .....	17
Figure 2.6. Differential scanning calorimetry heating curve of $[\text{N}_{\text{ip}311}][\text{Tf}_2\text{N}]$ .....	20
Figure 2.7. Differential scanning calorimetry curves of $[\text{N}_{10,111}][\text{Tf}_2\text{N}]$ , $[\text{N}_{10,111}][\text{beti}]$ , and $[\text{Pr}_{10,1}][\text{beti}]$ .....	22
Figure 2.8. Crystal structure of $[\text{N}_{12,111}][\text{Br}]$ .....	26
Figure 2.9. Wide-angle X-ray scattering of $[\text{N}_{10,111}][\text{Br}]$ , $[\text{N}_{10,111}][\text{Tf}_2\text{N}]$ , $[\text{N}_{10,111}][\text{beti}]$ , and $[\text{Pr}_{10,1}][\text{beti}]$ .....	26
Figure 2.10. Isothermal aging of $[\text{N}_{10,111}][\text{beti}]$ X-ray scattering data at 17 °C .....	28
Figure 2.11. Carbon-deuterium bond against a magnetic field and a Pake doublet .....	30
Figure 2.12. $^2\text{H}$ NMR lineshape data of DTAB- $\text{d}_{21}$ .....	32
Figure 2.13. Isothermal aging of DTAB- $\text{d}_{21}$ $^2\text{H}$ NMR lineshape data at 17 °C and 10 °C.....	32
Figure 2.14. Comparison of DTAB- $\text{d}_{21}$ lineshape against nonadecane- $\text{d}_{40}$ and deuterated polyethylene.....	33
Figure 2.15. Cisoid and transoid conformations of $[\text{beti}]^-$ .....	35

Figure 2.16. Temperature dependent infrared spectra of $[N_{10,111}][\text{beti}]$ .....	36
Figure 2.17. Arrhenius plot of relative infrared peak heights for $[N_{10,111}][\text{beti}]$ .....	37
Figure A.1. Temperature calibration for 300 MHz and 500 MHz NMR instruments using methanol and ethylene glycol .....	46
Figure A.2. Comparison of diffusion coefficients between pulsed field gradient NMR and molecular dynamics simulations.....	47
Figure A.2. Comparison of experimental pulsed field gradient diffusion coefficients against literature and simulation values .....	48
Figure A.3. Solid-echo NMR pulse sequence.....	49

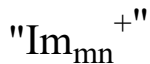


## List of Tables

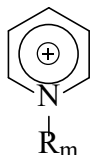
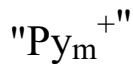
Table 2.1. Calorimetric Data for $[\text{N}_{10,111}][\text{beti}]$ , $[\text{Pr}_{10,1}][\text{beti}]$ , and $[\text{N}_{10,111}][\text{Tf}_2\text{N}]$ .....	22
Table 2.2. X-ray scattering $q$ ranges .....	25
Table 2.3. Summary of solid phases .....	42

## Ionic Liquid Nomenclature

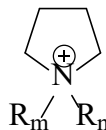
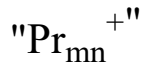
### Cations



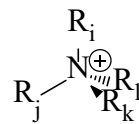
imidazolium



pyridinium

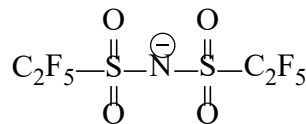
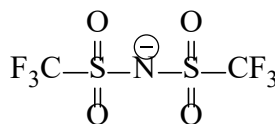
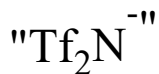
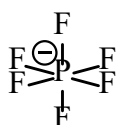
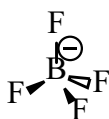


pyrrolidinium



ammonium

### Anions



Nomenclature used to denote ionic liquid components in this thesis: Ionic liquids are designated according to cation type Im, Py, P, and N together with numbers indicating the length of appended n-alkyl chains, i, j, k, l. Ionic liquids are labeled [cation][anion]. For example, [Im<sub>41</sub>][BF<sub>4</sub>] is 1-butyl-3-methylimidazolium tetrafluoroborate.

## Chapter 1: Rotation in Ionic Liquids

### 1.1 Introduction

Ionic liquids (ILs), defined as salts with melting temperatures at or below 100 °C, have many favorable properties such as low vapor pressure, high thermal stability, and are generally chemically inert<sup>1</sup>. ILs have a lot of potential for various applications because their viscosity, density, and other physical properties are tunable through selection of the cation and anion pair or through modification of the functional groups appended to these ions. For example, ILs tuned for low viscosity could be used as green solvents for reactions<sup>2</sup> and battery electrolytes<sup>3</sup>. To properly utilize ILs, and guide the best choice of cation and anion, a fundamental understanding of their properties is necessary. As a means of probing the friction operating on solutes undergoing reactions, we have studied rotational dynamics in the prototypical ionic liquid 1-butyl-3-methylimidazolium tetrafluoroborate ([Im<sub>41</sub>][BF<sub>4</sub>]) and its mixtures with a polar protic solvent.

## 1.2 Solute Rotation in Ionic Liquids

I contributed to two projects that focused on the rotational diffusion of solutes in the ionic liquid [Im<sub>41</sub>][BF<sub>4</sub>]. A combination of molecular dynamics (MD) simulations and NMR T<sub>1</sub> relaxation experiments were conducted to elucidate the molecular origins of friction on rotational motion in ionic liquids. These two studies are now published as Refs 4 and 5.

In the MD simulations, rotations of molecules can be directly observed in model systems. In such a model the cations, anions, and solute molecules are objects with defined properties such as size, shape, and partial charge. These molecules are initially equilibrated, and then classical trajectory data is collected over hundreds of nanoseconds. To characterize rotations from these trajectories in an average manner appropriate for comparison to experiment, rotational time correlation functions (RTCFs), are calculated.

$$C_{rot}^{(2)} = \frac{3}{2} \langle \hat{u}(0) \cdot \hat{u}(t) \rangle^2 - \frac{1}{2} \quad (1)$$

In this expression  $\hat{u}$  is the direction of some particular bond within a molecule and the brackets indicate averaging over like molecules and time. The RTCF characterizes the timescales of different motions involved in rotation<sup>6</sup>. It decays from 1 at  $t = 0$  down to 0 at long times. By fitting this decay, time constants for the rotational motion can be extracted.

NMR can experimentally access the rotations of molecules through observation of nuclear spin relaxation. For an NMR active nucleus, the rotation of the molecule is weakly coupled to the relaxation of the nuclear spins. There are multiple mechanisms for the relaxation of nuclear spins such as dipole-dipole interactions, chemical shift anisotropy, and quadrupolar interactions. Here I will discuss the case of deuterium spin relaxation, in which case, the quadrupolar interactions dominate the relaxation of a deuterium spin characterized by a spin-lattice relaxation time T<sub>1</sub><sup>7</sup>.

$$T_1^{-1} = \frac{3\pi^2}{10} \left( 1 + \frac{1}{3} \eta_Q^2 \right) \chi^2 (j(\omega_0) + 4j(2\omega_0)) \quad (2)$$

Values of  $\eta_Q$  and  $\chi^2$ , the asymmetry parameter and the quadrupole coupling constant respectively, were calculated for each species studied using electronic structure calculations<sup>4</sup>.  $T_1$  relates to rotation occurring at the Larmor frequency, ( $\omega_0$ ) and its overtone ( $2\omega_0$ ) because  $j(\omega)$  in Eq 2 is the spectral density of rotational motion.

$$j(\omega) = \int_0^\infty C_{rot}^{(2)}(t) \cos(\omega t) dt \quad (3)$$

Seen in Equation 3, the spectral density function is the Fourier transform of the RTCF, the function output by the MD simulations. By measuring the  $T_1$  relaxation time, we have a point of comparison to validate the MD simulations. There is an additional result seen in Equation 3. The spectral density function is frequency dependent. The  $\cos(\omega t)$  term can be reduced to a constant if the value  $\omega t$  does not change for the range of the RTCF. In this case the spectral density terms reduce to the integral rotation time ( $\tau_{rot}$ ), i.e.  $\tau_{rot} = j(0) = \int_0^\infty C_{rot}^{(2)}(t) dt$ . This simplification provides

$$T_1^{-1} = \frac{3\pi^2}{10} \left(1 + \frac{1}{3}\eta_Q^2\right) \chi^2 \tau_{rot} \text{ when } \tau_{rot}\omega_0 \ll 1. \quad (4)$$

in which there is an inverse relationship between the  $T_1$  time and  $\tau_{rot}$ . The region where the condition  $\tau_{rot}\omega_0 \ll 1$  holds is termed the extreme narrowing limit. This region provides for easy comparison between the MD simulation and experiment, but the frequency dependent behavior is lost, yielding only an averaged rotation time. The two rotational diffusion projects I worked on used  $^2\text{H}$   $T_1$  measurements within the extreme narrowing limit to simplify interpretation of the NMR data.

## 1.3 Solute Dynamics in an Ionic Liquid

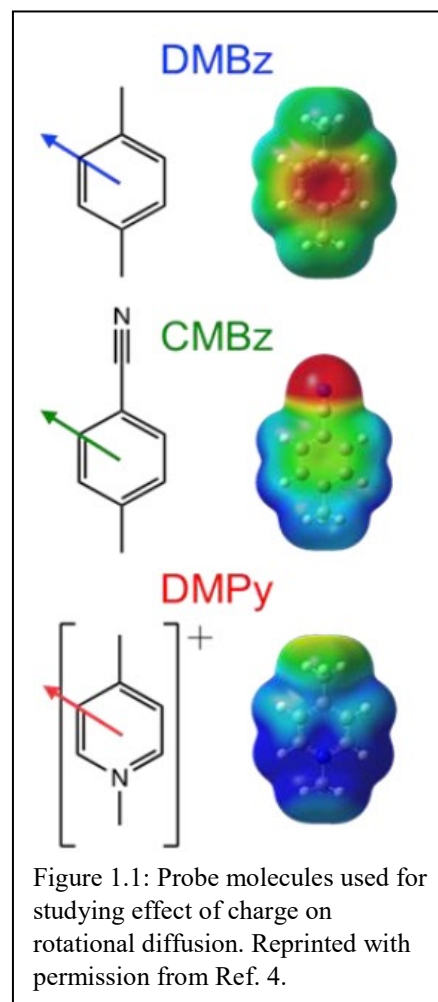
### A. Experimental:

The three probe molecules investigated with NMR are shown in Figure 1.1. Nonpolar dimethylbenzene- $d_{10}$  (DMBz), in blue, and dipolar cyanomethylbenzene- $d_7$  (CMBz), in green, were purchased (CDN Isotopes, 99 atom%). Charged dimethylpyridinium- $d_7$  was synthesized by Chris Rumble, detailed in Ref 4. Samples were prepared containing ~50 mM probe in [Im<sub>41</sub>][BF<sub>4</sub>]. The ionic liquid was initially placed under vacuum until the water content was <100 ppm, the probe was added, and the solution was transferred to an NMR tube and flame-sealed to prevent moisture from reentering the system.

An Avance III-HD 500 MHz NMR equipped with a Prodigy BBO cryoprobe was used for  $T_1$  measurements.  $^2\text{H}$

NMR measurements of liquid samples employed the lock channel of the instrument, which meant that weaker and longer excitation pulses than ideal were required. The  $T_1$  experiment uses two pulses: a  $180^\circ$  pulse to invert the net magnetization, and a  $90^\circ$  pulse to allow for signal detection after the evolution period. The pulse duration was calibrated through a series of single pulse experiments of varying duration using the ‘popt’ command.

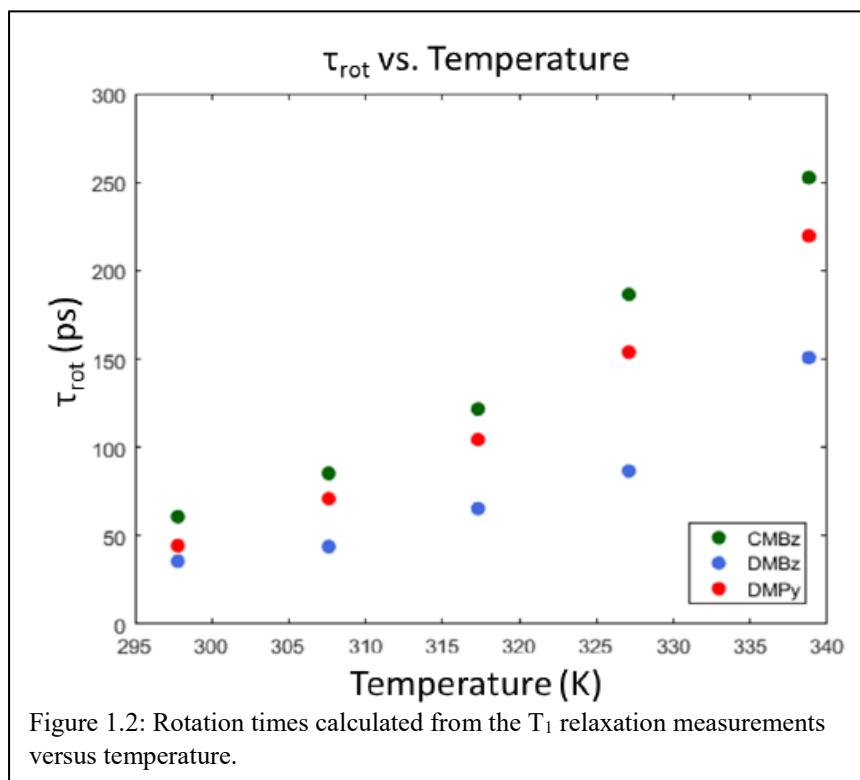
The pulse sequence used was a deuterium inversion–recovery pulse sequence spanning 4 orders of magnitude or more in recovery time for the determination of longitudinal relaxation times. The amplitude of the deuterium signal was fit to an exponential recovery curve and 3 replicates were used. Recycle delays were set at 5 seconds for complete recovery of magnetization.



The temperature calibration is covered in Sec. A.1. The arrow on each molecule in Figure 1.1 gives the vector accessed through the NMR experiment, i.e. the aromatic deuterons for each probe.

## B. Results and Discussion:

Figure 1.2 shows the rotation times as temperature was varied from 297–338 K. DMBz has the fastest rotation, followed by DMPy, and finally CMBz. Intuitively, one might expect the order from fastest to slowest to be DMBz, CMBz, then DMPy, i.e. ordering solutes from nonpolar,



dipolar, to charged. Instead we observe ordering of nonpolar, charged, to dipolar. This reflects the subtle differences in the interactions of localized solute charges with the solvent ions. DMPy has the greatest total interaction with the solvent because it has a net charge. The local environment of DMPy is a shell consisting predominantly of anions. CMBz however has a dipole that is localized to the cyano-group. The local environment consists of both positively and negatively charged areas oriented around the molecule. Rotation of the molecules requires a larger local environmental response in CMBz than DMPy, leading to a slower rotation time for CMBz than DMPy.

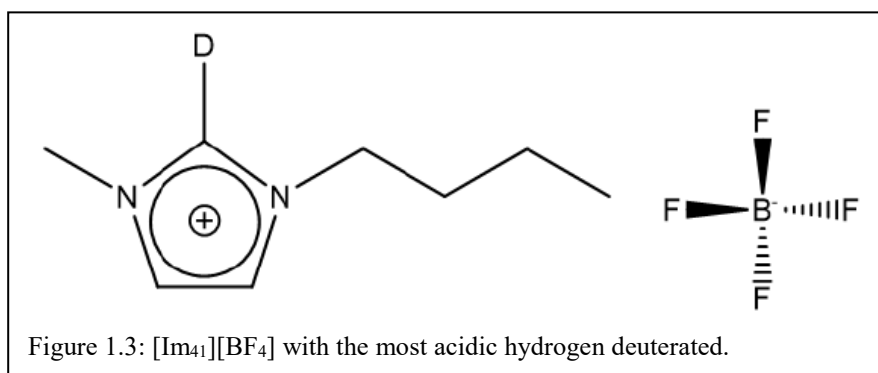
## 1.4 Solute and Solvent Dynamics in an IL and Acetonitrile Mixture

### A. Introduction:

The second system I studied was the mixture of  $[\text{Im}_{41}][\text{BF}_4]$  with acetonitrile (ACN). The high viscosities of many ILs limit their utility as solvents for synthesis and as electrolytes in batteries, because it limits the rate of reactant and charge transport. One option to overcome this limitation is to mix the IL with a less viscous conventional solvent, enhancing the fluidity of the ionic liquid, but often still retaining many of the IL's desirable properties. The binary mixture  $[\text{Im}_{41}][\text{BF}_4] + \text{ACN}$  is completely miscible at room temperature<sup>8</sup>, making it a useful prototype of an ionic + dipolar aprotic liquid mixture with which to investigate how rotational and translational motion change with changing composition and viscosity. Brian Conway performed MD simulations of the solvent mixtures from neat ACN to neat  $[\text{Im}_{41}][\text{BF}_4]$  with and without benzene as a solute. I performed complimentary NMR  $T_1$  measurements; this work is detailed in Ref 5.

### B. Experimental:

Deuterated ACN was purchased in small ampules from Cambridge Isotope Laboratories and opened just before sample preparation to minimize



water contamination.  $[\text{Im}_{41}][\text{BF}_4]$  was deuterated at the single site shown in Figure 1.3 following a procedure of a previous group member, Anne Kaintz<sup>8</sup>. The C(2) proton of the imidazolium ring is the most acidic proton and was found to exchange when  $[\text{Im}_{41}][\text{BF}_4]$  is refluxed in 9:1  $\text{D}_2\text{O}:\text{H}_2\text{O}$  for eight hours. Deuteration was checked via  $^1\text{H}$  NMR by measuring the relative depletion of peak

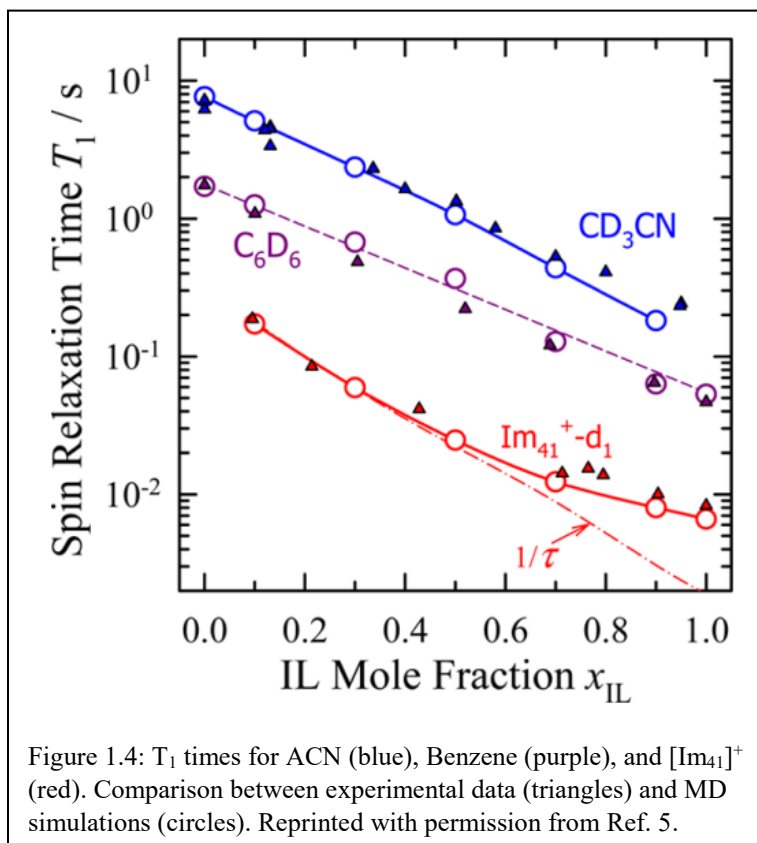


intensity before and after deuteration. This process achieved ~20% deuteration of the C2 carbon and no detectable deuteration at the other carbon positions. The ionic liquid was then heated to ~50 °C and dried under vacuum until the water content was <100 ppm as measured by Karl Fisher. The deuterated ACN was purchased in ampules from Cambridge Isotope Laboratories and opened just before sample preparation to minimize water content. The components were weighed separately and combined into NMR tubes, which were then flame-sealed to prevent evaporation of ACN and uptake of water by the ionic liquid.

Because the relaxation times of acetonitrile, benzene, and the imidazolium cation were typically very different, separate sets of delay times were used in this experiment to capture the behavior of each component.

### C. Results and Discussion:

The comparison between experimental  $T_1$  times (triangles) and simulated values (circles) is shown in Figure 1.4. Acetonitrile  $T_1$  times are in blue, the  $[\text{Im}_{41}]^+$  cation times in red, and the benzene solute times in purple. The ordering of the three molecules follows size, as ACN is the smallest, followed by benzene, and the largest and slowest is the  $[\text{Im}_{41}]^+$  cation. Benzene was chosen as a



solute because it provided a natural extension of previous work by Chris Rumble and Anne Kaintz

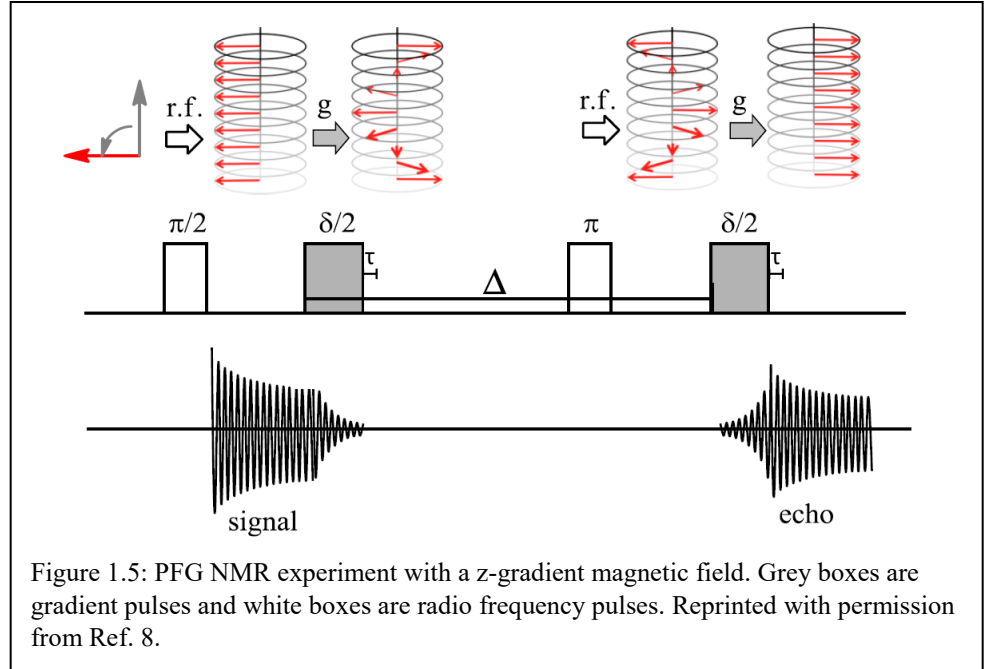
using MD simulations and NMR  $T_1$  relaxation measurements in  $[\text{Im}_4][\text{BF}_4]$ <sup>6</sup>. It is interesting that there is an approximate power law relationship between the  $T_1$  times and the viscosity of the solution. One could expect for a mixture between two dissimilar solvents that as the composition changes, the solvents do not mix completely; instead the solvents would form into regions with a higher concentration of one solvent as is observed in mixtures of ionic liquids with water<sup>9</sup>. These  $T_1$  data do not appear to indicate anything but nearly ideal mixing.  $T_1$  times measured using NMR for the two solvents as well as the solute of benzene agree reasonably with the simulated times over the span of the sampled viscosities, which provides confidence in the choice of parameters used to model the mixture.

Closely related to rotation times are translational diffusion rates. Using the simulation trajectories, translational diffusion coefficients for the two solvents and benzene were also calculated and compared with pulsed field gradient (PFG) NMR measurements. Calculation of the diffusion coefficients ( $D$ ) from the MD simulations followed Equation 5.

$$D = \frac{1}{6} \lim_{t \rightarrow \infty} \frac{d}{dt} \langle (\vec{r}(t) - \vec{r}(0))^2 \rangle \quad (5)$$

It is straightforward to follow the positions of molecules as a function of time,  $\vec{r}(t)$ , from which the squared displacement of each molecule can be tracked. Averaging this quantity over all molecules of a given type provides mean squared displacement  $\langle (\vec{r}(t) - \vec{r}(0))^2 \rangle$ . At short times, the mean squared displacement does not track diffusion because translational motion is dominated by small scale vibrational and librational motions of the molecules moving and impacting against adjacent molecules. Only at long times does the slope of the mean squared displacement over time, reflect the diffusion coefficient of the molecules.

The PFG NMR technique, shown in Figure 1.5<sup>8</sup>, uses a different approach than  $T_1$  relaxation to measure the translational diffusion coefficient. At the start of the PFG experiment, the net magnetization is aligned



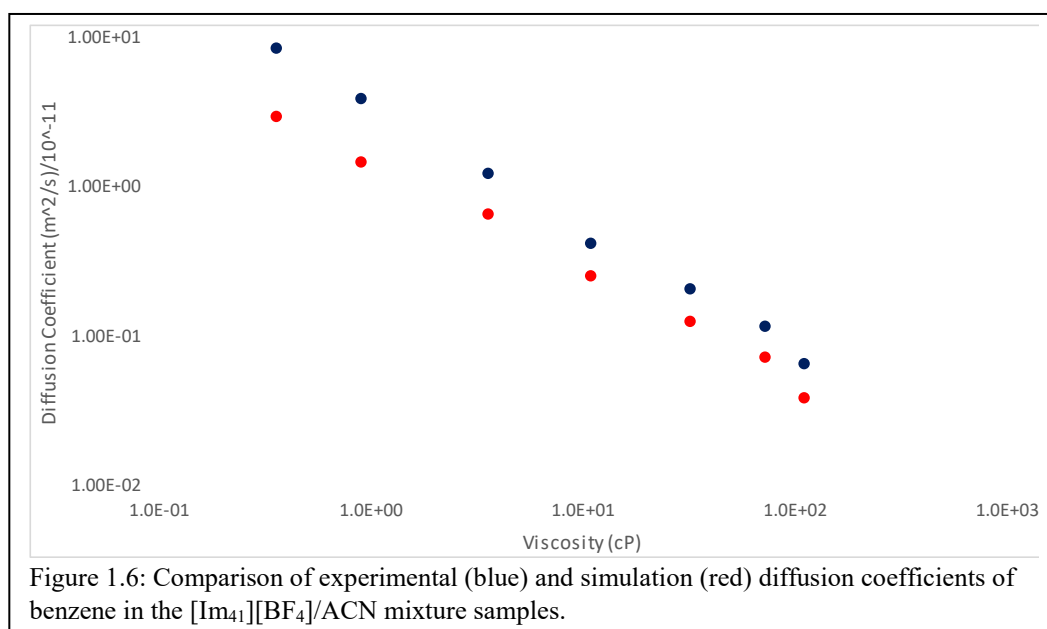
with the external magnetic field, or along the vertical z-axis in Figure 1.5. A radio frequency (r.f.) pulse is applied that rotates the net magnetization 90°, into the xy-plane. This is followed by a gradient pulse to induce a gradient of the magnetic field with respect to the z-axis, essentially encoding the position of each spin along the z-axis. As the local magnetic field increases, it causes the transverse magnetization to precess at higher frequencies, as seen at the top of Figure 1.5 following the first “g” pulse. After a wait time ( $\Delta$ ), a second matching gradient pulse reverse the effects of the first gradient. If no diffusion occurred along the z-axis, this second pulse would completely reverse the effects of the first gradient pulse, causing no signal attenuation. If there is diffusion, the resulting NMR signal is attenuated in proportion to the distance moved. The relationship between the initial signal area ( $I(0)$ ) and the detected attenuated signal area ( $I(g)$ ) is provided by Equation 6.

$$I(g) = I(0) \exp \left\{ D(\gamma \delta g)^2 \left( \Delta - \frac{\delta}{3} - \frac{\tau}{3} \right) \right\} \quad (6)$$

$D$  is the diffusion coefficient, the value we use to compare between experiment and simulation. During the PFG experiment, there are two gradient pulses with a wait time between them ( $\Delta$ ). The gradient pulse duration ( $\delta$ ), and the gradient pulse intensity ( $g$ ) can be varied to determine the diffusion coefficient. The gyromagnetic ratio ( $\gamma$ ) is dependent on the nucleus selected. Gradient pulses cause electrical eddy currents that add artifacts and noise to the spectrum,  $\tau$  is the wait time to allow these eddy currents to relax before any subsequent pulse is applied. For our experiments,  $\Delta$  and  $\delta$  were held constant as  $g$  was varied to characterize the attenuation due to diffusion.

The comparison between MD simulated diffusion coefficients (red) and experimentally measured values (blue) is shown in Figure 1.6. The separation between the data is not a constant factor as there is a larger separation between experiment and simulation for the low viscosity data than the high viscosity data. The simulation data agrees with previously published diffusion coefficients published by Liang *et al.*<sup>10</sup> It has been determined the NMR diffusion coefficients were incorrectly measured as the gradient strength ( $g$ ) was incorrectly reported during these measurements. Section A.2 details the steps taken to calibrate the PFG NMR experiment. Future

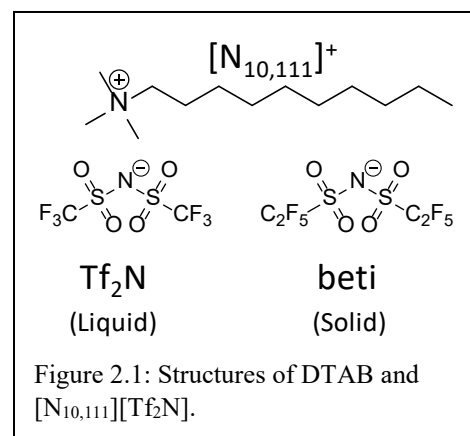
PFG NMR measurements should utilize an external standard for scaling of the diffusion coefficients to a literature value.



## Chapter 2 [N<sub>10,111</sub>][beti] a Distinctive Ionic Solid

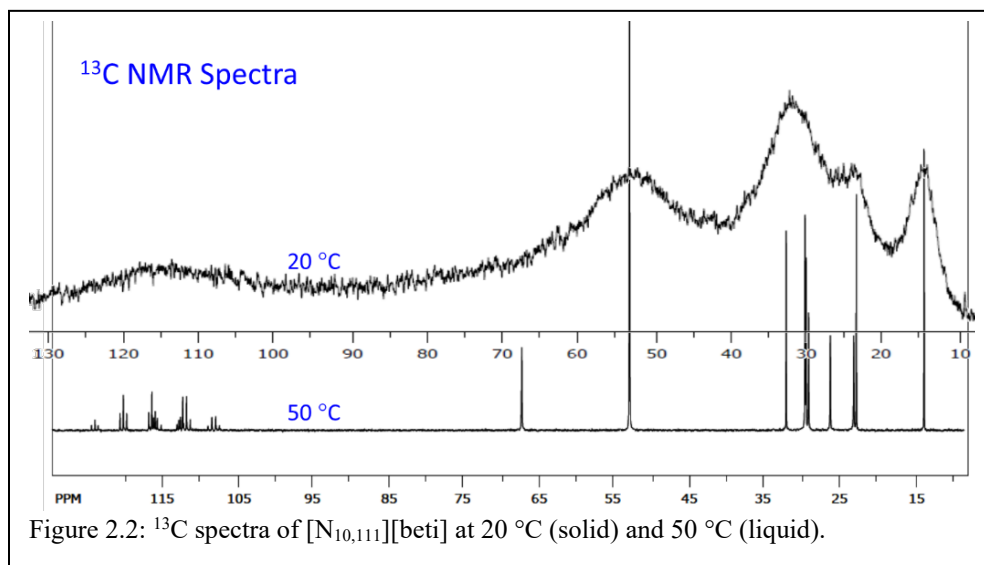
### 2.1 Introduction

The structure of DTAB is seen in Figure 2.1. DTAB is an ionic liquid with a melting temperature of 31 °C, making it an optically clear solid at room temperature. No other ionic liquid known forms an optically clear room-temperature solid of this sort; ionic liquids tend to form glasses at much lower temperatures or polycrystalline solids near room temperature. When the DTAB anion is substituted for [N(SO<sub>2</sub>CF<sub>3</sub>)<sub>2</sub>]<sup>-</sup>, ([Tf<sub>2</sub>N]) also shown in Figure 2.1, the ionic liquid persists in the liquid phase to a much lower temperature, forming a crystalline solid near -30 °C<sup>11</sup>. The unique nature of the solid phase of DTAB spurred initial nuclear magnetic resonance (NMR) and X-ray diffraction (XRD) experiments that were used when deciding on a framework for further analyses of DTAB.



#### A. Preliminary NMR Data:

Figure 2.2 shows preliminary <sup>13</sup>C NMR spectra of DTAB collected by a former student Bernie O'Hare in 2009. The top spectrum is at 20 °C, in the solid phase, and the spectrum on the bottom is at 50 °C, in the liquid. The 50 °C spectrum, with



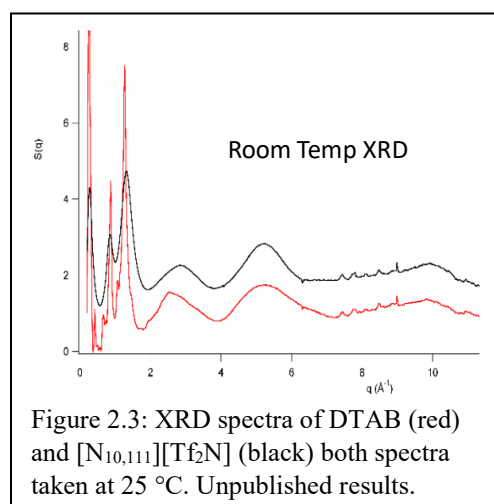
its sharp well-separated resonances, is typical of a spectrum of a liquid of small molecules. The

spectrum of the solid shows much broader peaks, but many of the peaks are still resolved. Solid-state systems typically produce much broader and less resolved spectra because molecular level motions are no longer fast on the NMR timescale<sup>12</sup>. The fact that the  $^{13}\text{C}$  spectrum of DTAB in the solid-state shows some resolution indicates the presence of motional narrowing greater than is typical in a glassy or crystalline solid. Such motional narrowing is the result of molecular motions within the solid phase of DTAB that I've attempted to characterize using NMR, as described in Sec 2.5.

## B. Preliminary X-ray Data:

Several years ago, Edward Castner Jr. our collaborator at Rutgers University, took the X-ray diffraction (XRD) data shown in Figure 2.3. DTAB is plotted in red and  $[\text{N}_{10,111}][\text{Tf}_2\text{N}]$  in black. These XRD spectra were taken at room temperature where DTAB is a solid and  $[\text{N}_{10,111}][\text{Tf}_2\text{N}]$  a liquid. The spectra show the scattered intensity as a function of momentum transfer,  $q$ , defined by  $q = (4\pi/\lambda)\sin\theta$  where  $\lambda$  is the x-ray wavelength and  $\theta$  is the scattering angle. Large  $q$  corresponds to intramolecular distances while small  $q$  are intermolecular distances.

Narrow peaks in the XRD spectrum indicate a highly ordered structure like that expected for a crystal. Broad peaks indicate amorphous structure characteristic of a liquid or glass. Both DTAB and  $[\text{N}_{10,111}][\text{Tf}_2\text{N}]$  have broad intramolecular peaks. For lower  $q$ , the intermolecular scale,  $[\text{N}_{10,111}][\text{Tf}_2\text{N}]$  has additional broad peaks while the peaks of DTAB are sharper and more distinct, indicating



some degree of crystallinity in the solid phase of DTAB. It is unusual that both crystalline and amorphous structure are present in the solid phase.

The preliminary NMR and X-ray data suggest that the solid phase formed by DTAB is unusual. The research in this chapter is aimed to explore that nature of the solid in more detail.

## 2.2 Types of Solids

Solid phases of molecular compounds range from glassy to crystalline solids. A crystalline solid is: “a crystal structure is a regular arrangement of atoms of molecules.<sup>13</sup>” Additionally, the average position of an atom within the crystal structure does not change with time. A crystalline solid is well ordered and it takes substantial energy is usually required to change a crystalline solid to a liquid. On the other end is the glassy solid. Glassy solids are amorphous solids where the arrangement of atoms or molecules is random and disordered, like a liquid. A glass to liquid state transition requires less energy than a crystal to liquid transition because there is less ordering in the solid phase.

The preliminary data from XRD indicates that DTAB is not simply an amorphous solid or an ordered solid, but a superposition of both. The NMR data indicates that there is significant motion occurring into the solid phase of DTAB. In this thesis, I will discuss three different types of solids: plastic crystals, glacial solids, and Frank-Kasper phases as possible frameworks for understanding the structure and dynamics of DTAB. The general features of these solids are described below.

### A. Plastic Crystals:

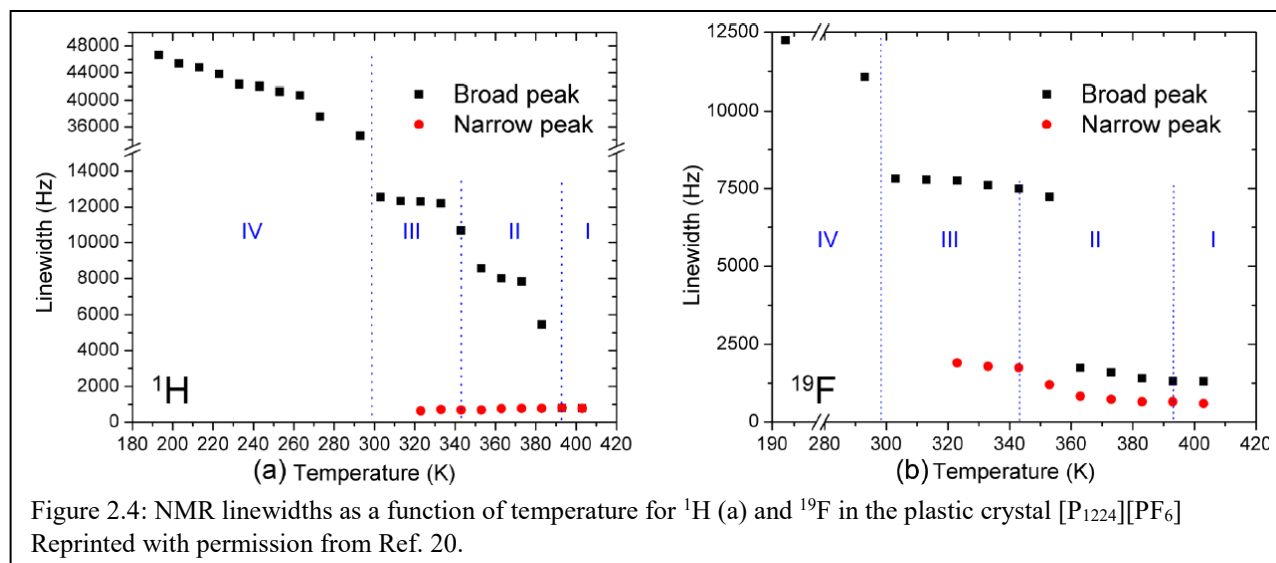
The classification “plastic crystal” stems from the fact that some organic crystals, particularly those comprised of quasi-spherical molecules, have high plasticity<sup>14</sup> rather than being brittle, as is the case for “normal” organic crystals. Plastic crystals possess long-range translational order but are orientationally disordered. Typically, a plastic crystalline phase is not the only solid phase formed by a compound. Plastic crystals are often observed to undergo multiple solid-solid phase transition; they form crystalline solids at lowest temperatures and different rotational motions become less restricted as temperature is increased. The enhancement of orientational and



rotational motions as temperature is increased can be a sudden process, reflected in a phase change, or a gradual process. In either case, the entropy changes from plastic crystal to liquid or between two plastic crystalline phases are smaller in magnitude than the entropy change between a crystalline solid and a liquid. For this reason, Timmerman proposed one metric for determining whether a compound is a plastic crystal is that it possesses a low entropy of fusion ( $<20 \text{ J K}^{-1} \text{ mol}^{-1}$ )<sup>15</sup>.

The dynamics within a plastic crystal are often complex. Cyclohexane, as discussed in a paper by McGrath *et al.* provides an entry point<sup>16</sup>. Cyclohexane forms a single plastic crystalline phase between  $-87^\circ\text{C}$  and its melting point,  $6^\circ\text{C}$ . McGrath and Weiss considered three mechanisms for the dynamics within cyclohexane: rotational, translational, and conformational. They measured  $^1\text{H}$ ,  $^{13}\text{C}$ , and  $^2\text{H}$  lineshapes as a function of temperature. The different nuclei experienced changes to their lineshapes at different temperatures within the plastic crystalline phase of cyclohexane. Through an analysis of the different relaxation mechanisms involved for the different nuclei, McGrath *et al.* determined time scales for the motions of cyclohexane, most notably rotation of molecules occurring on  $\mu\text{s}$ -ns time scales.

More recent examples of plastic crystals include organic ionic plastic crystals (OIPCs). OIPCs are ionic compounds made from imidazolium<sup>17</sup>, phosphonium<sup>18</sup>, and ammonium<sup>19</sup> cations usually combined with smaller inorganic anions that form plastic crystals in the solid state. Jin *et al.* studied the OIPC  $[\text{P}_{1224}][\text{PF}_6]$ <sup>20</sup>. Differential scanning calorimetry (DSC) showed this compound to undergo 4 solid-solid phase transitions between the well-ordered crystal and the liquid. Jin *et al.* used NMR lineshape measurements to examine the rotational motion within the solid phases. An advantage of studying the compound ( $[\text{P}_{1224}][\text{PF}_6]$ ) was that hydrogen and fluorine are only contained in the cation and anion respectively, which enabled Jin *et al.* to observe



their motions independently. They found that some of the phase changes produced abrupt linewidth changes in either the hydrogen or fluorine peaks, as shown in Figure 2.4. This behavior indicates motion of the cation or anion are primarily involved in each transition. Jin *et al.* observed four solid phases of  $[P_{1,224}][PF_6]$  labeled I-IV where IV is the lowest temperature solid phase. In the NMR spectra, there are two changes observed. At low temperatures, there is a broad peak that gradually narrows as the temperature increases. Additionally, a narrow peak appears on top of the broad peak, indicating a growing fraction of  $[P_{1,224}][PF_6]$  is in a less restricted environment. Phase IV shows a gradual decrease in the  $^1H$  and  $^{19}F$  linewidth. Jin *et al.* connect this to rotation of the methyl and ethyl groups of the cation and isotropic tumbling of the anion respectively. The transition to phase III produces linewidth jumps for both nuclei. This is attributed to rotation of the cation around an individual axis. Phase II produces a dramatic change in the fluorine linewidth while the change to hydrogen is less dramatic. Jin *et al.* connect this to diffusive motion of the anion while the cation rotation is gradually becoming less restricted. The final solid-solid phase transition to phase I does not have significant change in the fluorine lineshape as it is already diffusive motion. The broad peak of the hydrogen disappears as the cation also undergoes diffusive motion. NMR lineshape was used by Jin *et al.* to obtain a detailed understanding of molecular

motions in an ionic compound. Similar measurements will be useful to characterize the molecular motions of DTAB.

## B. Glacial States:

Glacial states consist of nanocrystallites imbedded in an amorphous phase. These states may be formed when crystallization occurs near the glass transition, creating conditions in which only nm-scale crystallites can be formed before further growth of the crystallites is halted. Glacial states have only been clearly identified in a small number of systems. One of the most studied examples is triphenyl phosphite (TPP). Guinet *et al.* used low-frequency Raman spectra to characterize the glacial state formed by TPP forms under specific temperature protocols.

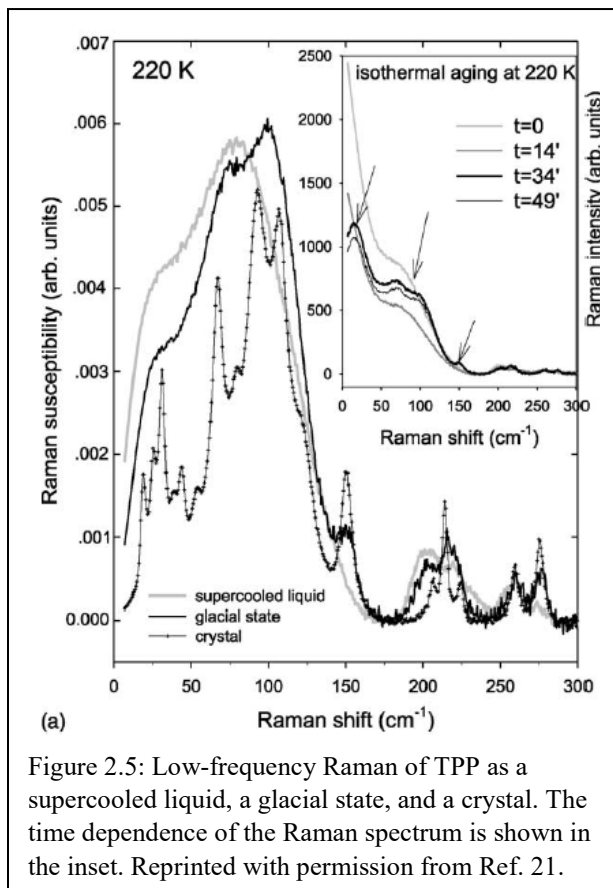


Figure 2.5: Low-frequency Raman of TPP as a supercooled liquid, a glacial state, and a crystal. The time dependence of the Raman spectrum is shown in the inset. Reprinted with permission from Ref. 21.

One method of forming the glacial state of TPP is to hold it isothermally at 220 K, ~20 K above the glass transition temperature. Figure 2.5, from the paper by Guinet *et al.*, demonstrates the mixed nature of the glacial state<sup>21</sup>. The glacial state spectrum contains both broad and sharp peaks, indicative of the amorphous and crystalline phases respectively. Additionally, the inset shows development of the crystalline peaks over the course of an hour as the glacial state develops from isothermal aging.

The only ionic compound so far reported to form a glacial phase is  $[N_{4111}][Tf_2N]$  by Faria *et al.*<sup>22</sup>  $[N_{4111}][Tf_2N]$  formed the glacial phase through two temperature protocols: rapid cooling

followed by slow heating, and isothermal aging. Faria *et al.* used Raman spectroscopy to characterize the conformations of the  $\text{Tf}_2\text{N}^-$  anion, which can adopt into cisoid and transoid forms. If the solid formed were a single crystal, only a single form of the anion is expected. The solid phase formed by  $[\text{N}_{4111}][\text{Tf}_2\text{N}]$  through the isothermal aging method primarily adopted the cisoid conformation, but the transoid conformation was present as well.

### C. Frank-Kasper Phases:

Frank and Kasper originally observed FK phases in metal alloys<sup>23</sup>. Elemental metals typically adopt body-centered cubic (BCC) or face-centered cubic (FCC) structures, which have 2 and 4 atoms per unit cell, respectively. In contrast, many metal alloys composed of 2 or more elements adopt much more complex structures having anywhere from 12 up to 30 atoms per unit cell. Driving the formation of these more complex FK structures is the desire to achieve topological close packing (TCP) where the structures that have TCP have exclusively tetrahedral interstices<sup>13</sup>. Packing in this manner can achieve a lower total energy than the other arrangements when the main interactions involve central potentials.

In addition to alloys, FK phases have recently been found to occur in systems of simple aqueous surfactants<sup>24</sup> and neat diblock copolymers<sup>25</sup>. The surfactants and diblock copolymers form into micelles that then organize into FK phases. In both the surfactant and the diblock copolymer systems, FK phases were detected using small-angle X-ray scattering (SAXS) analysis. In the SAXS spectra, numerous peaks are visible due to the large number of distinct sites in the unit cell. In the case of the diblock copolymer, the FK phases were formed via isothermal aging like the formation of the glacial state.

The three solid phases described above present comparisons for the analysis of DTAB. Plastic crystals, glacial states, and FK phases all form in systems composed of molecules similar

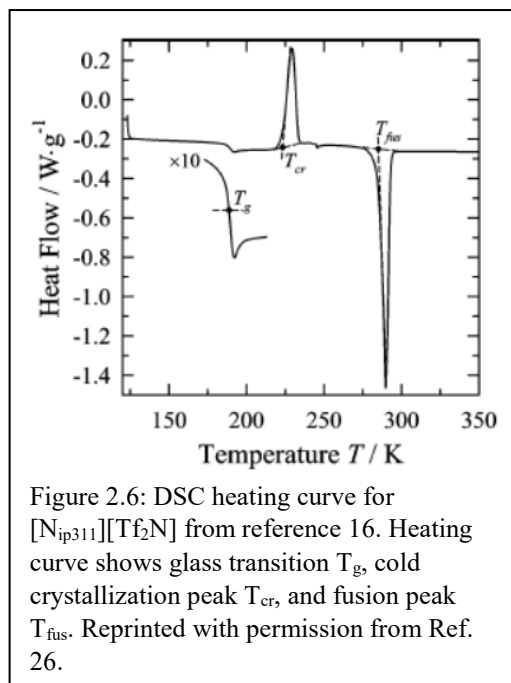
to  $[N_{10,111}][\text{beti}]$ . The spectroscopic techniques that are discussed in the remainder of this chapter include differential scanning calorimetry (DSC), X-ray scattering,  $^2\text{H}$  NMR, and infrared (IR) spectroscopy. DSC identifies the phase transitions and the temperatures of interest to help guide subsequent experiments with the other techniques. The X-ray scattering data is used in both plastic crystals and FK phases to examine the degree of ordering and identify the structure of the solid. NMR lineshapes have been used in plastic crystals to examine the dynamics within the solid and identify transitions in the motion. Infrared spectroscopy is used like Raman spectroscopy to examine the possibility of a glacial state. Isothermal aging is a key component in the formation of both the glacial state and the FK phases and is used in the NMR, X-ray, and IR analyses.

## 2.3 Differential Scanning Calorimetry

### A. Introduction:

DSC measurements provide a starting point for the characterization of DTAB. DSC compares the amount of heat required to change the temperature of a compound at a constant rate against a reference with a known heat capacity. Here and in almost all cases the reference is simply an empty pan. When the compound of interest undergoes a phase transformation, the amount of heat required differs from the reference. An endothermic phase transition requires more heat flowing to the sample to change the temperature at the same rate as the reference, whereas in an exothermic phase transition heat flows out of the sample. Another type of transition is a glass transition, signaled by an inflection point in the DSC curve, indicating an abrupt change in the heat capacity of the sample. Data can either be collected upon heating or cooling the sample, but a complete experiment includes both the heating and cooling curves.

Figure 2.6 shows a representative DSC curve of the ionic compound  $[\text{N}_{\text{ip}311}][\text{Tf}_2\text{N}]$ , taken from a previous Maroncelli group paper<sup>26</sup>. The baseline heat flow is negative, indicating that it is a heating curve. There is an inflection point below 200 K, indicative of a glass transition. The temperature of this transition ( $T_g$ ) is taken at the inflection point. At 225 K there is an exothermic peak indicative of crystallization of the sample. The two important pieces of information about such a peak are the temperature of the transition ( $T_{\text{cr}}$ ),



and the enthalpy of the transition.  $T_{\text{cr}}$  is determined from the onset of the transition. For this heating

curve,  $T_{cr}$  is measured from the left side of the peak at the point where the left slope intersects the baseline. The enthalpy of the transition is the area under the curve multiplied by the calorimetric constant, which is instrument dependent. The third peak near 280 K is an endothermic peak indicative of fusion of the sample. The temperature of fusion ( $T_{fus}$ ) and enthalpy of fusion are determined in the same way as for the crystallization peak.

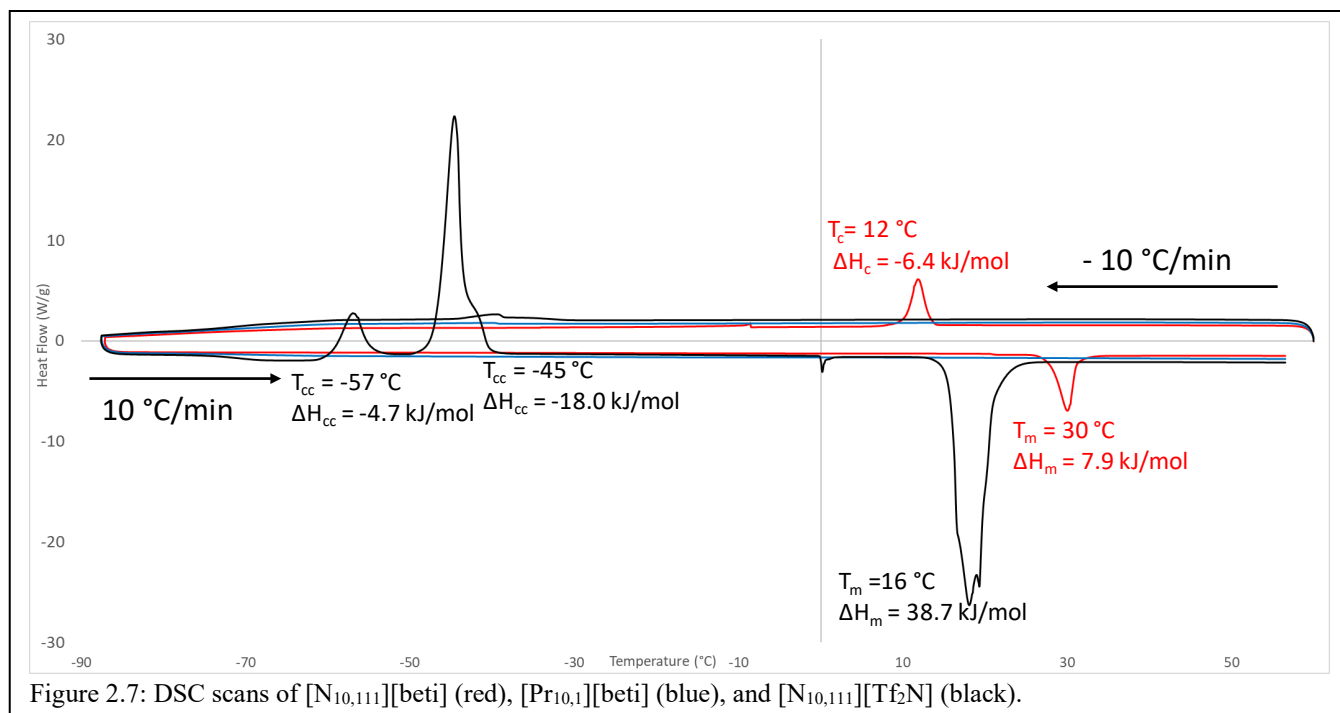
As illustrated in Figure 2.6, the temperature at which a sample crystallizes may be far removed from the temperature at which it melts. This hysteresis is a kinetic effect in samples that are readily supercooled. The extent of the hysteresis depends on the rate of heating and cooling. A slower rate should reduce the size of the hysteresis. For a more complete understanding of the behavior of a compound, multiple rates of temperature ramping should be used.

## B. Experimental:

Data was collected on a TA Instruments Q2000 Modulated Differential Scanning Calorimeter. The pans used to hold the samples and serve as a reference were “Tzero” aluminum pans. Compounds studied were  $[N_{10,111}][beti]$ ,  $[N_{10,111}][Tf_2N]$ , and  $[Pr_{10,1}][beti]$ . Samples were melted prior to placing them in the sample pan. The heating/cooling protocol brought the sample to 60 °C then cooled to -90 °C at 10 °C/min. The sample was then heated back to 60 °C at 10 °C/min. Table 2.1 contains the sample weights. Only single DSC scans of  $[N_{10,111}][Tf_2N]$  and  $[Pr_{10,1}][beti]$  collected to date. DTAB scans are similar to scans obtained by our collaborators Jim Wishart and Bratoljub Milosavljevic.

## C. Results:

DSC curves of DTAB and two other ionic liquids,  $[Pr_{10,1}][beti]$  and  $[N_{10,111}][Tf_2N]$ , used for comparison are shown in Figure 2.7. Transition data are compiled in Table 2.1. DTAB ( $[N_{10,111}][beti]$ ) (red curve) has a relatively simple DSC scan. There is a single peak in the cooling run,



indicating a liquid to solid phase transition. The heating run shows a single peak for the solid-to-liquid transition. There is a hysteresis of about 18 °C where DTAB is in a supercooled liquid state. The ionic liquid  $[N_{10,111}][Tf_2N]$  (black curve) has a few more features in the DSC scan. In the cooling curve there is no crystallization peak, just a change in heat flow near -45 °C which is not

**Table 2.1: Calorimetric Data**

Ionic liquid	$T_{cr}\text{ °C}$	$\Delta_{cr}H$ $\text{kJ mol}^{-1}$	$T_{fus}\text{ °C}$	$\Delta_{fus}H$ $\text{kJ mol}^{-1}$	$\Delta_{fus}S$ $\text{kJ mol}^{-1}\text{ K}^{-1}$	Sample weight (mg)
$[N_{10,111}][beti]$	12	6.37	30	7.94	0.026	5.7
$[Pr_{10,1}][beti]$	—	—	—	—	—	6.8
$[N_{10,111}][Tf_2N]^1$	-57, -45	4.69, 18.00	16	38.71	0.13	7.6

$T_{cr}$ ,  $\Delta_{cr}H$ ,  $T_{fus}$ , and  $\Delta_{fus}H$  are the temperatures and enthalpies of crystallization and fusion. <sup>1</sup>The crystallization temperatures for  $[N_{10,111}][Tf_2N]$  were measured upon heating whereas those of  $[N_{10,111}][beti]$  were measured upon cooling.

consistent with crystallization at lower temperature upon heating. On the heating curve there are two exothermic peaks indicative of cold crystallization. Upon further heating a melting peak is observed.



$[N_{10,111}][Tf_2N]$  provides a point of comparison with Mizuhata *et al.* as they examined a series of  $[N_{n,111}][Tf_2N]$  ionic liquids via DSC<sup>11</sup>. My values for the melting point and entropy of fusion ( $\Delta_{fus}S$ ) are 16 °C and 0.13 kJ mol<sup>-1</sup> K<sup>-1</sup> respectively, which are comparable with values reported by Mizuhata *et al.* of 23 °C and 0.16 kJ mol<sup>-1</sup> K<sup>-1</sup>. In examining where their DSC curve intersects the baseline for  $[N_{10,111}][Tf_2N]$ , their melting point is also ~16 °C. Comparison of the cold crystallization peaks shows that on subsequent heating/cooling cycles, there is a single cold crystallization peak. Multiple peaks are likely due to the sample not being uniform within the aluminum pan and thus separate portions of the sample undergo the phase changes at slightly different temperatures.

The third ionic liquid  $[Pr_{10,1}][beti]$  does not have apparent melting or crystallization peaks. Jin *et al.* report that there is a glass transition near -80 °C in  $[Pr_{10,1}][Tf_2N]$ <sup>26</sup>.

DTAB sits between the other two ionic liquids in terms of the phase changes. It has crystallization and melting peaks unlike  $[Pr_{10,1}][beti]$ , but the entropy of these transitions are much lower than those seen in  $[N_{10,111}][Tf_2N]$ . The  $\Delta_{fus}S$  is 0.026 kJ mol<sup>-1</sup> K<sup>-1</sup> for DTAB which is five times less than for  $[N_{10,111}][Tf_2N]$  at 0.13 kJ mol<sup>-1</sup> K<sup>-1</sup>. The difference in magnitude between the two compounds indicates a difference in the degree of ordering in the solid phase. The larger the entropy difference, the higher the degree of ordering in the solid phase. DTAB has a lower degree of ordering than  $[N_{10,111}][Tf_2N]$  by a significant margin. The value of 0.026 kJ mol<sup>-1</sup> K<sup>-1</sup> is comparable to Timmerman's observation about plastic crystals (<0.02 kJ mol<sup>-1</sup> K<sup>-1</sup>)<sup>15</sup>. The DTAB DSC results are consistent with measurements taken by our collaborators Jim Wishart and Bratoljub Milosavljevic. More measurements are being performed. Additional experiments examining the scan rate are planned as one of the key identifiers of the glacial phase is a variation in the solid formed based on scan rate<sup>22</sup>.

## 2.4 X-ray Scattering

### A. Introduction:

Multiple techniques fall under the term X-ray scattering. All are used to characterize the spatial structure of materials. A beam of monochromatic X-rays interacts with a sample. The X-rays are scattered by the electrons in the sample and the measured interference pattern yields information about the sample's atomic structure. Sharp, well defined peaks indicate a more well-ordered system, whereas broad and less intense peaks indicate a more disordered system. Scattering at small angles/scatter vectors  $q$  reflect intermolecular distances and large  $q$  reflects intramolecular distances. Lattice spacings  $d$  are related to  $q$  by  $d = 2\pi/q$ .

To examine the possibility that the DTAB solid should be viewed as a type of FK phase, a glacial state, or a plastic crystalline phase, markers in the X-ray scattering data are required. In the case of FK phases a significant time dependence is often found for their formation. For example, Lee *et al.* observed that block copolymer systems that form FK phases first order into a body-centered cubic (BCC) structure during the first 5 hours of isothermal aging<sup>25</sup>. As aging continued, the BCC peaks decay away and are slowly replaced by the final FK phase. It is unclear what timescale to expect for similar changes in the DTAB system.

The formation of a glacial state should also be accompanied by a time evolution in the data. Faria's work on the glacial state of  $[N_{4,111}][Tf_2N]$  does not include X-ray scattering, but the Raman data indicates formation of nanocrystallites during isothermal aging that should be visible by XRD<sup>22</sup>. These nanocrystallites occur over a range of sizes and are embedded in an amorphous phase, producing a complicated X-ray scattering pattern. The X-ray studies of the glacial state formed by TPP show a  $q^{-4}$  dependence at  $q < 0.04 \text{ \AA}^{-1}$  ( $d > 150 \text{ nm}$ ) due to the presence of a distribution of nanocrystal sizes<sup>27</sup>.

Plastic crystals are typically more crystalline than a glacial state or FK phase. X-ray scattering experiments reflect this, as the data can be fit to crystal structures<sup>19</sup>. One common aspect of plastic crystals is that multiple solid-solid phase transitions are often visible as peaks in the DSC. The different solid phases organize into different crystal structures<sup>17</sup>, which is reflected in different sets of peaks at different temperatures in the X-ray scattering data.

X-ray scattering experiments were performed using a Xenocs Xeuss 2.0 instrument, equipped with microfocus sealed tube (copper) with an X-ray wavelength of 1.54 Å (50 kV, 0.6 mA). Scattering data were collected under vacuum. Samples were prepared in 1 mm diameter quartz capillaries and sealed with epoxy. Two instrumental setups were used to obtain different scattering vector ( $q$ ) ranges. For each setup the overall  $q$  range observable depended on the number of images collected. These ranges are given in Table 2.2. Exposure times were 300 seconds except

<b>Table 2.2: X-ray Scattering Ranges</b>					
Small angle X-ray scattering (SAXS)			Wide angle X-ray scattering (WAXS)		
Min. $q$ (Å <sup>-1</sup> )	Max. $q$ (Å <sup>-1</sup> )	Images	Min. $q$ (Å <sup>-1</sup> )	Max. $q$ (Å <sup>-1</sup> )	Images
0.008	0.236	1	0.10	1.68	1
0.008	0.400	2	0.10	2.60	2
0.008	0.480	3	0.10	2.90	3

the 60 °C and the initial 17 °C SAXS spectra of DTAB, which had an exposure time of 60 seconds per image. The 2D images were converted into one-dimensional plots of scattering intensity  $I(q)$  (arbitrary units) versus  $q$  by integrating semicircular portions of the images.

## B. Results:

Four ionic compounds were examined in X-ray scattering experiments:  $[N_{10,111}][\text{beti}]$  (DTAB),  $[N_{10,111}][\text{Tf}_2\text{N}]$ ,  $[\text{Pr}_{10,1}][\text{beti}]$ , and  $[N_{10,111}][\text{Br}]$ . The bromide was added as a reference because it is a high-melting solid expected to have a well-ordered crystal structure similar to the structure published for the homologous compound  $[N_{12,111}][\text{Br}]$ <sup>28</sup>.

In the case of crystalline  $[N_{12,111}][Br]$ , shown in Figure 2.8, cations organize into sheets of all trans  $C_{12}$  chains. The cation heads alternate with  $Br^-$  anions to form a polar region and the alkyl tails remain mostly trans but with a small twist and fill a nonpolar domain between the polar regions.

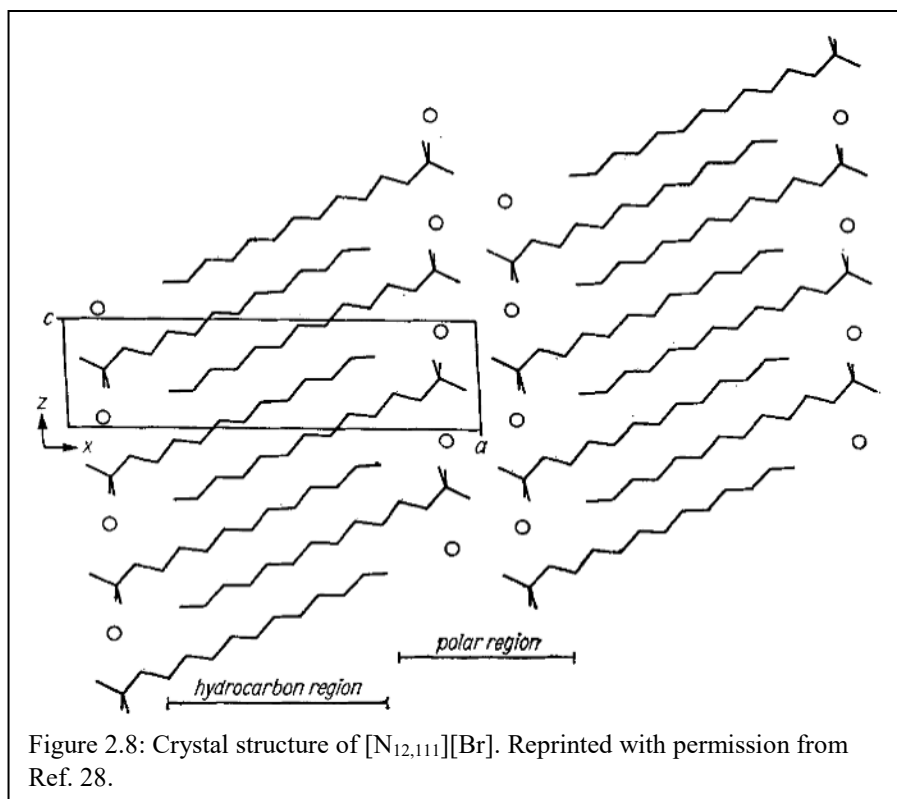


Figure 2.9 compares the X-ray scattering patterns of the four compounds. The  $[N_{10,111}][Br]$  data were recorded at 25 °C, because it has a melting point above 200 °C. The  $[N_{10,111}][Tf_2N]$  and  $[Pr_{10,1}][beti]$  data were taken at -60 °C, which is below  $T_{cr}$  of the  $[Tf_2N]$  ionic liquid (-57 °C).

$[Pr_{10,1}][beti]$  is likely a supercooled liquid at this temperature.  $[N_{10,111}][beti]$  data were taken at 25 °C after an isothermal aging process, discussed in Sec. C, and having been cooled to low temperature. The  $[N_{10,111}][Br]$  spectrum, in

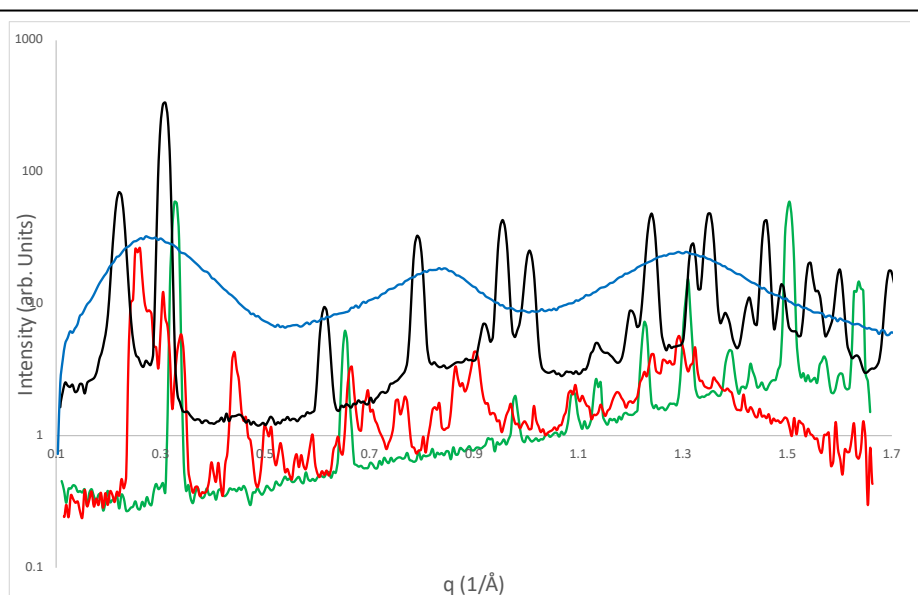


Figure 2.9: WAXS spectra of  $[N_{10,111}][Br]$  (green),  $[N_{10,111}][Tf_2N]$  (black),  $[N_{10,111}][beti]$  (red), and  $[Pr_{10,1}][beti]$  (blue).

green, shows peaks that are sharp and well defined. It is expected that the crystal structure of  $[N_{10,111}][Br]$  should be similar to that of the known structure of  $[N_{12,111}][Br]$ , with the main difference being that the size of nonpolar domains would be slightly smaller. Initial attempts to fit the unit cell parameters to the scattering pattern observed for  $[N_{10,111}][Br]$  yielded several possibilities similar to the  $[N_{12,111}][Br]$  case.

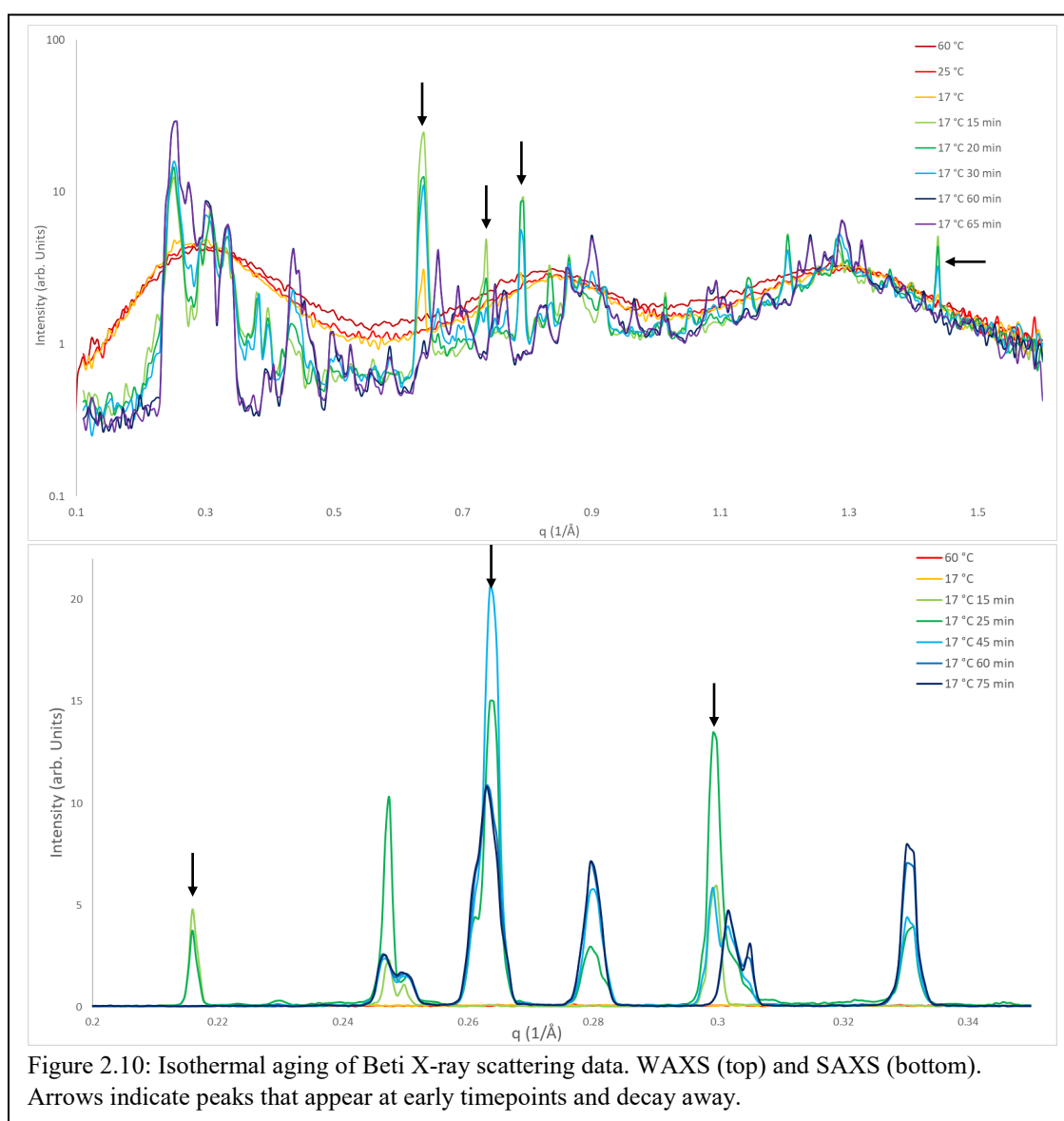
There is a clear difference between the powder patterns shown by  $[N_{10,111}][Br]$  (green),  $[N_{10,111}][Tf_2N]$  (black), and the two beti compounds (red and blue). Both the  $[Tf_2N]$  and  $[Br]$  compounds have sharp, well defined peaks at regular intervals, indicating a high degree of order.  $[N_{10,111}][beti]$  (DTAB) in red has a much higher number of overlapping peaks, indicating there is order, but the order is not regular throughout the sample.  $[Pr_{10,1}][beti]$  in blue on the other hand shows only 3 broad peaks common to most ionic liquids<sup>29</sup>. These broad peaks indicate  $[Pr_{10,1}][beti]$  is either a liquid or a glass and remains largely disordered at -60 °C.

These observations agree with the DSC results in that the much larger fusion entropy of  $[N_{10,111}][Tf_2N]$  compared to DTAB suggests a much more ordered solid. While sharp peaks in the DTAB spectrum indicate substantial order, the broad underlying scattering indicates substantial amorphous character as well.

### C. Time Evolution of DTAB

Figure 2.10 includes multiple temperatures and a time evolution of DTAB to elucidate the formation of the solid. The top panel shows data recorded using the WAXS setup and the bottom panel the SAXS setup. The 60 °C data (dark red) displays three broad peaks characteristic of ionic liquids and similar to the  $[Pr_{10,1}][beti]$  data in Figure 2.9 (blue). This was the starting point for the set of experiments; DTAB in the liquid state. Similar broad peaks are visible in the 25 °C (red) and initial 17 °C (orange) spectra. The initial 17 °C spectrum includes small sharper peaks, the most

visible forming near  $0.6 \text{ \AA}^{-1}$  in the WAXS data. The remainder of the data was collected while holding temperature at  $17^\circ\text{C}$ . The 15, 20, and 30-minute timepoints show growth of sharp, relatively isolated peaks indicated by arrows as well as growth of areas of overlapping peaks throughout the  $q$  region scanned by WAXS. Interestingly, the peaks indicated by arrows in the WAXS data disappear after the 30-minute timepoint, indicating changes in the lengthscale of the structure forming within DTAB and could reflect a different organizational structure. The overlapping sets of peaks, particularly the grouping around  $0.3 \text{ \AA}^{-1}$ , tend to continue growing in



intensity to the 60 and 65-minute timepoints. This is more expected for a liquid changing to a solid, the peaks grow in intensity as a larger percentage of the compound adopts the final structure.

There are similar results in the SAXS data where peaks labeled with arrows grow in over the first 30 minutes but disappear before the 60-minute mark. SAXS also provides a rough estimate of the lattice spacings within DTAB as  $d = 2\pi/q$ . The smallest  $q$  peaks are approximately at 0.21, 0.25, and 0.26  $\text{\AA}^{-1}$ , which reflect distances of  $\sim 30$ , 25, and 24  $\text{\AA}$  respectively. 30  $\text{\AA}$  is a reasonable size for a single micelle but is smaller than a supermolecular ordering of micelles as is expected in FK phases. No small angle scattering was observed below the peak at 0.21  $\text{\AA}^{-1}$ . Thus, the  $q^{-4}$  dependence expected in the formation of a distribution of crystallite sizes is not observed.

## 2.5 $^2\text{H}$ NMR

### A. Introduction

In Chapter 1, I discussed the use of deuterium NMR  $T_1$  measurements to aid in understanding rotational motion in ionic liquids<sup>4</sup>. Deuterium NMR is also a useful tool in understanding motion in solid systems<sup>30</sup>, but there is much less freedom of motion in solids. Interactions that are typically averaged in a liquid, such as electric quadrupolar and magnetic dipolar interactions, now depend on molecular orientation within the solid<sup>12</sup>. This causes a substantial broadening of the spectrum. Deuterium has a nucleus of spin 1 and so, in the presence of a magnetic field, has three energy levels corresponding to spin quantum numbers  $m_z = +1, 0$ , and  $-1$  and two single-quantum transitions among these levels.

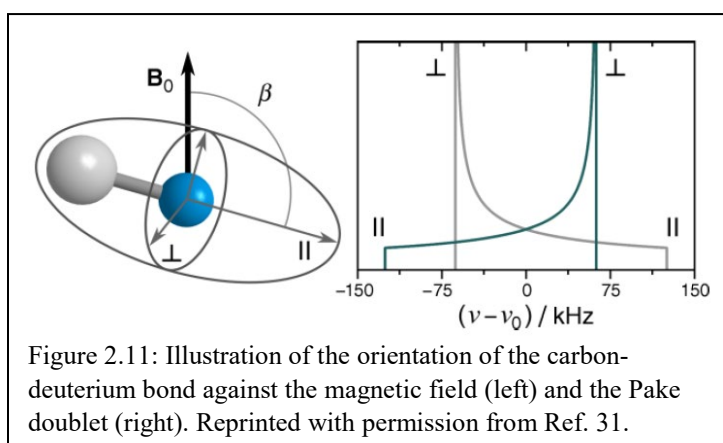


Figure 2.11: Illustration of the orientation of the carbon-deuterium bond against the magnetic field (left) and the Pake doublet (right). Reprinted with permission from Ref. 31.

The shape of the  $^2\text{H}$  spectrum indicates the nature of the solid phase. A crystalline solid comprised of immobile molecules all oriented in a similar manner has two Lorentzian peaks from the two allowed transitions. A powder sample also has two peaks, but each peak is broadly distributed as seen in Figure 2.11<sup>31</sup>. This pattern is due to the various alignments different crystals adopt relative to the instrument's magnetic field. This line shape is called a Pake pattern, and is typical of powder samples<sup>32</sup>. The splitting of the peaks in the Pake pattern is significant. In the absence of molecular motion, The splitting between the outermost shoulders in a Pake doublet is  $3C_Q/2$  and the splitting between the prominent inner peaks is  $3C_Q/4$ , where  $C_Q$  is the quadrupolar coupling constant<sup>7</sup>.



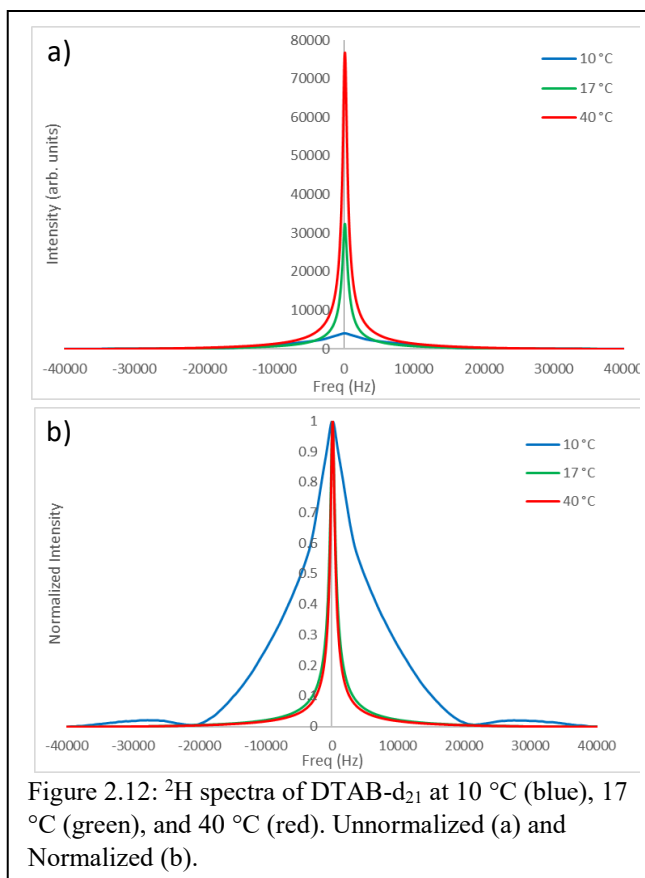
Solid-state NMR measurements were taken on an Avance-III-HD solid state 500 MHz instrument with a quadruple-tuned 4-mm cross polarized magic angle spinning (CPMAS) probe. Samples were paced in 4 mm rotor tubes with a Vespel cap and held immobile as the NMR spectra were collected. Spectra were recorded using a spin-echo pulse sequence, which involves two R.F. pulses to rotate the net magnetization. Two pulses are used due to the rapid decay of the net magnetization in the solid state. The initial  $90^\circ$  pulse rotates the net magnetization into the detectable window, followed by a  $30\ \mu\text{s}$  delay time before the second  $90^\circ$  pulse which refocuses the net magnetization. The magnetization refocuses based on the delay time and acquisition can collect the refocused echo, enhancing the signal in comparison to a single pulse probe experiment. 1024 scans were used for all spectra, and a sweep width of 156 kHz was used to observe the entire width of the Pake pattern, resulting in a spectrum taking 200 seconds to collect. Details on the calibration of experimental parameters are discussed in Sec. A.3. The sample used for  $^2\text{H}$  lineshape measurements,  $[\text{N}_{10,111}][\text{beti}]\text{-d}_{21}$  (DTAB- $\text{d}_{21}$ ) contained a perdeuterated decyl tail. It was synthesized by Gary Baker at the University of Missouri.

## B. Results

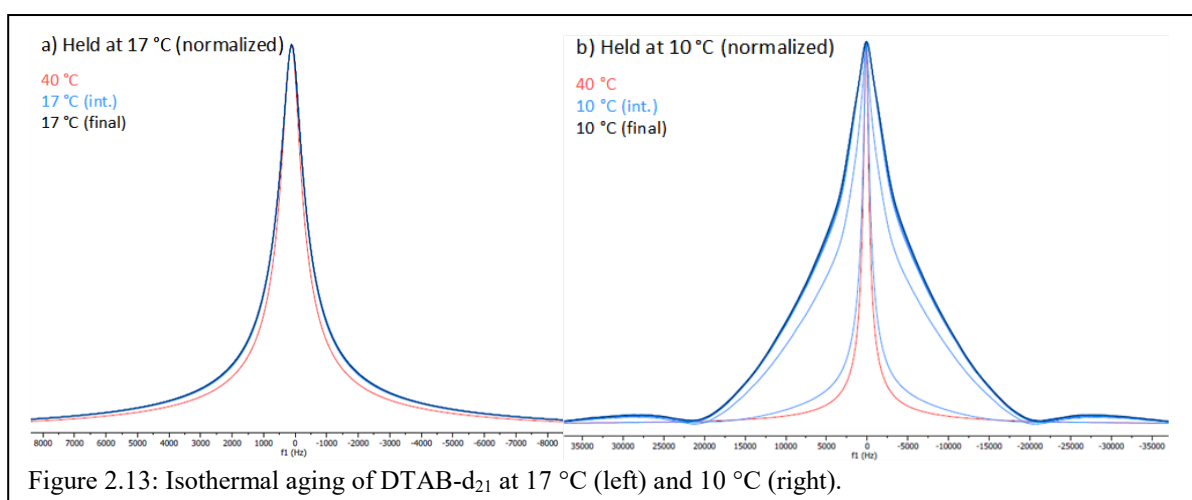
Presented in Figure 2.12a are  $^2\text{H}$  solid state spectra of DTAB- $\text{d}_{21}$  at 10, 17, and  $40\ ^\circ\text{C}$ . Calorimetric data indicate that the liquid-to-solid transition of DTAB occurs between 10 and  $17\ ^\circ\text{C}$  upon cooling, so two of the spectra are of the liquid state and one of the solid state. The peak in the solid spectrum ( $10\ ^\circ\text{C}$ ) is significantly broader, as seen in the normalized spectra of Figure 2.12b. Recent work on the ionic compound  $[\text{P}_{1224}][\text{PF}_6]$  provides some insight into the significance of the broadening upon solidification. The findings of Jin *et al.* are discussed in detail in sec. 2.3<sup>20</sup>. Jin *et al.* demonstrated that large-scale changes in the linewidths of  $^1\text{H}$  or  $^{19}\text{F}$  peaks at the phase changes of  $[\text{P}_{1224}][\text{PF}_6]$  reflect changes in the molecular motion of the cation or anion respectively.

In DTAB, a broadening of the deuterium peak reflects the fact that cation motion, specifically motion of the deuterated decyl tail, is markedly slowed as a result of solidification.

To elucidate the isothermal aging observed in the XRD experiments, analogous isothermal aging experiments were performed on DTAB-d<sub>21</sub>. The X-ray data showed structural equilibration was required to form a solid at 17 °C. Shown in Figure 2.13 are the normalized spectra of DTAB-d<sub>21</sub> during isothermal aging at 17 °C



(left) and 10 °C (right) after cooling from 40 °C. The 40 °C spectrum is shown in red in both cases.



The 17 °C series does not show significant change during the 60-minute experiment. The final linewidth is larger than at 40 °C, indicative of slowing of molecular motions, but no evolution of the lineshape is visible. At 10 °C there is a larger change that occurs over the course of multiple

scans as the line broadens into the final width after the first 6-10 minutes. This is interesting as the X-ray scattering saw development of peaks out to 60 minutes and some of the most dramatic changes occurred after 30 minutes.

### C. Discussion

Upon solidification, the  $^2\text{H}$  spectra of DTAB- $\text{d}_{21}$  do not form into a Pake doublet, the line shape expected when motion is significantly hindered on the microsecond time scale. Figure 2.14 compares the normalized DTAB- $\text{d}_{21}$  spectra against nonadecane- $\text{d}_{40}$  (“C19”) and deuterated polyethylene (“PE”) at several temperatures<sup>33-34</sup>. C19 exhibits two solid phases before melting at 32 °C.

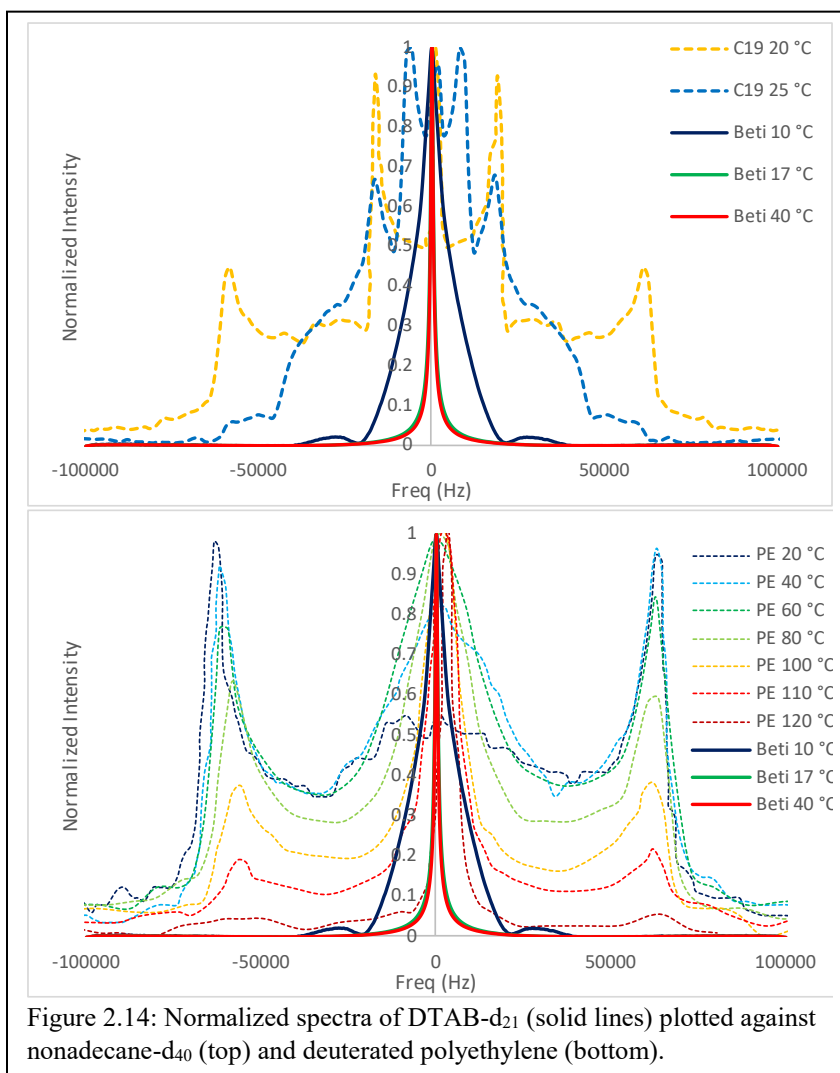


Figure 2.14: Normalized spectra of DTAB- $\text{d}_{21}$  (solid lines) plotted against nonadecane- $\text{d}_{40}$  (top) and deuterated polyethylene (bottom).

Below 22 °C (yellow), C19 exists in a crystalline structure wherein molecules organize into layers of all *trans* chains. At 25 °C (blue) C19 is termed a “rotator” phase, a type of plastic crystal having similar chain layering as the crystal but disordered orientations of the chains, which also include some gauche defects. In the C19 spectra of both phases, multiple sets of Pake doublets are visible.

In the 20 °C spectrum, the widest Pake doublet has a quadrupole splitting of 120 kHz while the narrower Pake doublet has a quadrupole splitting of 35 kHz. The narrower line collapses due to the rotation of the methyl group<sup>30</sup>. It is clear that the cation decyl chain of DTAB undergoes much more  $\mu$ s timescale motion than does C19 in its rotor phase.

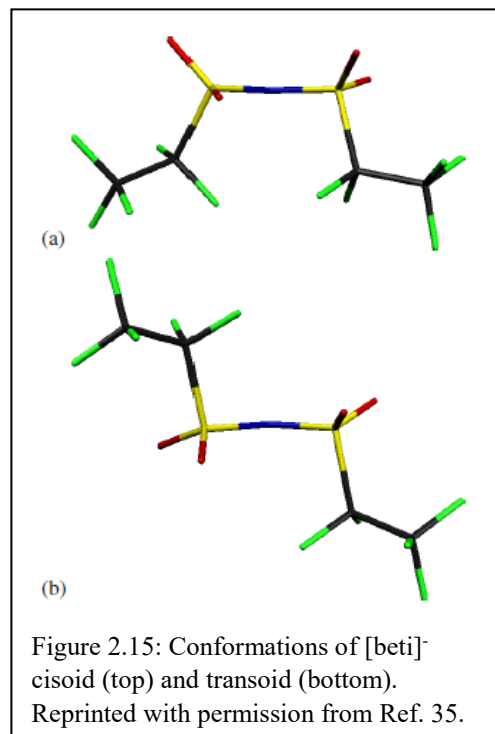
The PE spectra shown in the bottom panel of Fig 2.14 provides a more complete set of spectra for comparison. At 120 °C (dark red), near its melting point, PE contains a narrow, liquid-like spectrum superimposed over 2 broad, weak peaks at -60 and 60 kHz. These small peaks grow in prominence as the temperature is reduced, but a central liquid-like peak remains. This evolution reflects a fraction of PE is freely rotating at high temperatures and as the temperature is reduced, that fraction shrinks. It is unclear whether the spectrum of DTAB-d<sub>21</sub> at 10 °C reflects a similar phenomenon.

The solid-state spectrum of DTAB-d<sub>21</sub> reflects the disorder of the cation. Surprisingly, the motion of the decyl tail is sufficient to average the expected Pake pattern into a singlet peak at 17 °C, whereas X-ray scattering indicated the formation of ordering in the solid phase. Thus, the decyl tail is not involved in the formation of ordering seen in X-ray scattering.

## 2.6 Infrared Spectroscopy

### A. Introduction

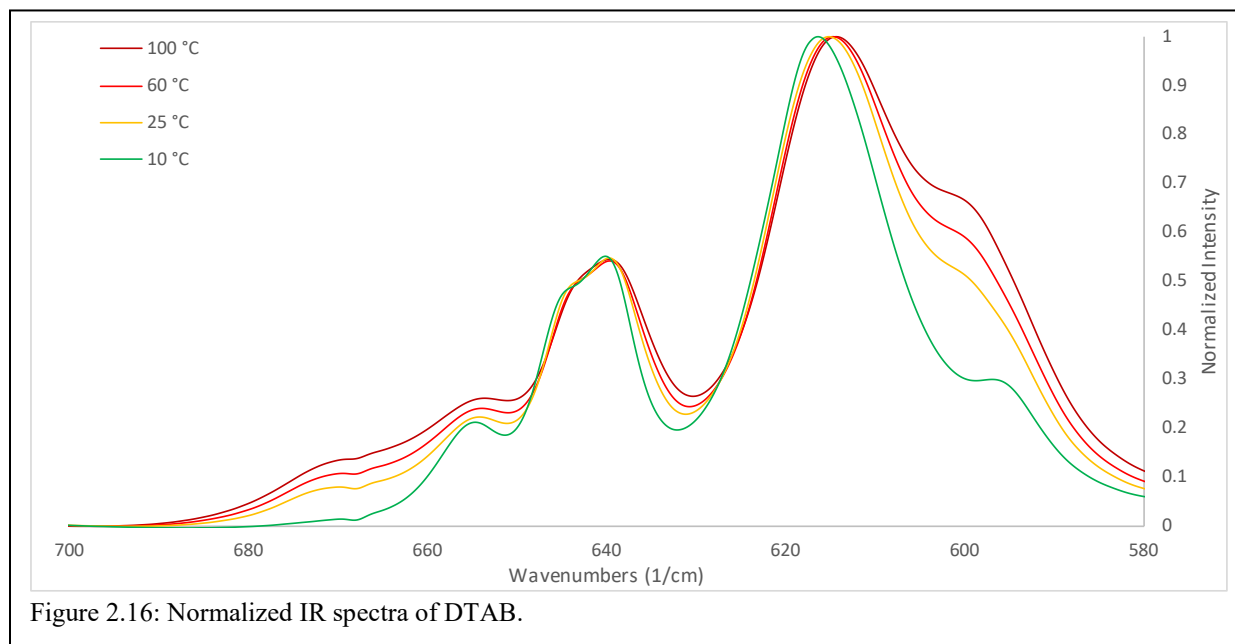
The IR data primarily provides a means to investigate cation and anion conformational changes. Shown in Figure 2.15 are the two conformers of the beti anion. Grondin *et al.* performed *ab initio* calculations as well as IR and Raman studies on [Li][beti] dissolved in glyme as well as [N<sub>1111</sub>][beti] to distinguish between the cisoid (top) and transoid (bottom) conformations<sup>35</sup>. *Ab initio* calculations indicate the transoid conformation is 6 kJ mol<sup>-1</sup> more stable than the cisoid conformation. Estimates based on the temperature dependence of beti band intensities in the 550–650 cm<sup>-1</sup> region in the IR spectrum yielded a similar value of 4.7 kJ mol<sup>-1</sup> for [Li][beti] dissolved in glyme. The cisoid and transoid conformations absorb at 601 and 615 cm<sup>-1</sup> respectively. As the temperature was reduced, the fraction of beti<sup>-</sup> anions in the transoid conformation increased. [N<sub>1111</sub>][beti] forms a crystal and IR spectra indicated all transoid conformation of the anion.



IR spectra were taken on a Bruker Vertex V70 IR spectrometer using a diamond ATR crystal. Spectra were recorded using 1 cm<sup>-1</sup> resolution over the range of 4000–550 cm<sup>-1</sup>.

## B. Results

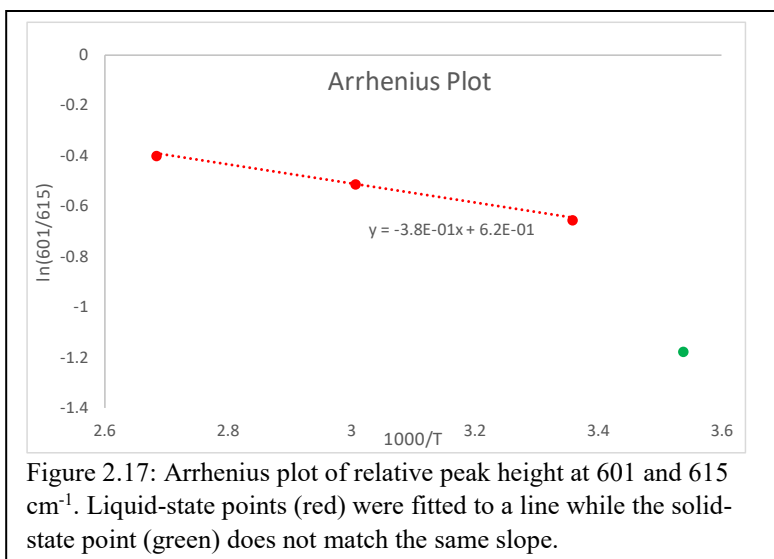
IR spectra of the region of interest are presented in Figure 2.16. Spectra were taken at four temperatures: 100 °C (dark red), 60 °C (red), 25 °C (orange), and 10 °C (green). The spectra are



shown normalized to the peak at  $615\text{ cm}^{-1}$ . There is an obvious decrease in the relative height of the  $601\text{ cm}^{-1}$  peak as the temperature decreases consistent with the observation of Grondin *et al.*<sup>35</sup>. There is also a large decrease in the relative intensity between the liquid spectrum at 25 °C and the solid spectrum at 10 °C.

These relative intensities are displayed in the form of an Arrhenius plot in Figure 2.17. From this plot, a preliminary estimate of  $\sim 4\text{ kJ mol}^{-1}$  is obtained for the energy difference between the cisoid and transoid conformations of the  $\text{beti}^-$  anion, comparable to the value found by Grondin *et al.* for  $[\text{Li}][\text{beti}]$  in glyme ( $4.7\text{ kJ mol}^{-1}$ ). Figure 2.17 also highlights the discontinuous change in the conformer ratio between the liquid and solid states. However, it is important to note that the presence of the  $601\text{ cm}^{-1}$  peak indicates a significant population of cisoid conformer persists in the

solid. After the 17 °C experiment, the IR temperature was set to 10 °C, which was reached within 5 minutes. IR experiments were run every 5 minutes for an hour and there were no changes in the IR spectra from the initial 10 °C spectrum. Thus the IR spectra, like



the NMR spectra did not exhibit the same slow relaxation (taking place over ~1 hour) that the XRD data did.

## 2.7 Discussion of the Nature of the DTAB Solid

The initial XRD and  $^{13}\text{C}$  NMR data suggested that the DTAB solid is something intermediate in order between a crystalline solid and an amorphous glass. In this thesis I consider three known types of solid that exhibit such an intermediate state of order: plastic crystals, glacial states, and FK phases. I now ask to what extent does the DTAB solid seem to fit into one of these three categories.

### A. Is the DTAB Solid a Plastic Crystal?

Plastic crystals are the most well studied of the three types of solids considered. The criteria for a plastic crystal are that a compound has translational order but rotational or orientational disorder. Based on the X-ray scattering data, DTAB does not seem to form a plastic crystal. The isothermal aging of DTAB at 17 °C demonstrated that order is forming in the supercooled liquid as it transitions slowly into the solid. The peaks grow in and decay within the isothermal aging. This indicates multiple structures are possible. Plastic crystals do adopt different structures as they go through solid-solid phase transitions, but do not exhibit the growth and decay of peaks during the isothermal aging. The number of peaks in the X-ray scattering data of DTAB does not appear to coincide with a single unique crystal structure for DTAB. Plastic crystalline compounds have translational ordering and the peaks can be fit to crystal structures.

$^2\text{H}$  NMR data is inconclusive. At 10 °C, the DTAB deuterium spectrum lacks a Pake doublet, indicating motion is still significant on the NMR timescale. The singlet peak that is present is significantly broadened in comparison to liquid-state data, indicating cation motion is markedly reduced in the solid. The broadening of the deuterium spectrum does not provide detailed information of the particular motions beyond the fact that it reorients the C-D bonds of the decyl



tail of the  $N_{10,111}^+$  cation. Additional experiments are required to isolate the specific motions slowed in the cooling process.

The IR data is also inconclusive in terms of the plastic crystalline phase. The IR data indicates that both conformations of the anion, cisoid and transoid, are present within the solid. If a well-ordered crystal was formed, I would expect only a single conformer to be present. The presence of both conformations indicates some disorder in the solid phase of DTAB, but it does not comment on the nature of the disorder.

## **B. Is the DTAB Solid a Glacial State?**

Glacial states consist of crystallites imbedded in an amorphous phase. In the case of triphenyl phosphite (TPP), the glacial state was formed through isothermal aging 20 °C above the glass transition temperature<sup>21</sup>. In DTAB, we observed structural changes via XRD as the system transformed from a supercooled liquid to a solid at 17 °C. Aspects of the XRD data support the formation of something akin to a glacial state. During the isothermal aging, order develops as indicated by sharp peaks growing in, like what is observed in TPP. I do not expect peaks to decay during isothermal aging in a glacial state; there is no indication that the crystallites forming in a glacial state would change between multiple structures. An additional consideration is the low q SAXS data. The formation of a distribution of quasi-spherical nanocrystallites of varying size should be accompanied by a  $q^{-4}$  dependence at low q. The lowest peaks observed in DTAB do not reflect the formation of crystallites as they occur near  $0.21 \text{ \AA}^{-1}$  ( $d \sim 25 \text{ \AA}$ ).

The  $^2\text{H}$  NMR data also do not support the formation of a glacial state. In such a state I would expect a superposition of a sharp liquid-like peak and a Pake doublet for the amorphous phase and the crystallites respectively. It is possible the amount of the crystalline phase is too small to be clearly visible, but that does not account for the isothermal aging component. In the XRD,

measurements at 17 °C were taken for 60 minutes. There were peaks growing in and decaying past 30 minutes. In the analogous  $^2\text{H}$  NMR experiments, the spectra were similarly collected for 60+ minutes, but no significant changes were seen after 3 minutes. This is an order of magnitude difference in the equilibration time of the XRD and  $^2\text{H}$  NMR. This suggests the  $\text{N}_{10,111}^+$  cations are not involved in the development of ordering seen in XRD.

The IR isothermal aging experiments do not reflect the formation of a glacial phase. Like the  $^2\text{H}$  NMR data, I would expect the IR data to reflect the development of ordering during the isothermal aging. The ratio of the two conformations does not change during the isothermal aging of the IR data. I would expect the formation of crystallites to be accompanied by a shifting of the ratio to the more favorable conformation in the crystallites.

### **C. Is the DTAB Solid Forming Frank-Kasper Phases?**

Observation of FK phases in soft-matter systems to date has involved packing of micellar structures. For DTAB to conform to this mold, it must first form micelles that then organize into the FK type structures. Additionally, in previously reported systems, there is XRD evidence that the micelles initially organize into a BCC structure and over time convert into the FK structure. In DTAB, the isothermal aging process sees initial sharp peaks that appear and decay away as many additional peaks grow in. One qualitative explanation is the initial BCC structure forms and then develops into the FK structure.

However, the SAXS data does not support identification of the DTAB solid as an FK phase. I envision the formation of micelles in DTAB would entail the  $\text{beti}^-$  anion plus cation heads forming the core of the micelle while the decyl tails of the  $\text{N}_{10,111}^+$  cation form the outer layer. It is unclear whether the alkyl portion of DTAB would be able to fill space between micelles, which puts the idea of FK phases in further doubt. More importantly, the lowest  $q$  peak observed in DTAB

is at  $q = 0.2 \text{ \AA}^{-1}$  ( $d \sim 25 \text{ \AA}$ ). This size is roughly consistent with the size of a micelle, but if large scale ordering occurs sharp peaks should form at lower  $q$  than in the liquid. Additionally, there may be a  $q^{-4}$  dependence, as is expected in a glacial state for the formation of crystallites, if micelles were forming. Overall, the XRD data yields some evidence for and against the formation of FK phases in DTAB.

It is more difficult to consider what the FK structure would appear as in the  $^2\text{H}$  NMR data. If the decyl tails make up the corona of the micelles, they would be rather fluid and would explain the absence of a Pake doublet. I would expect some arresting of motion during the isothermal aging as the micelles pack, but I did not find an example of NMR lineshapes in FK phases.

The IR data are consistent with a FK phase. IR indicates that the anion conformational equilibrium does not change during the isothermal aging. NMR indicates the cation does not reflect the order developing either. This suggests the ordering observed in the X-ray scattering is on a larger length scale than is picked up by the conformational changes seen by IR or the mobility of the alkyl chain observed by NMR. It is reasonable to conclude the ordering of micelles wouldn't be reflected in the NMR or IR data.

## 2.8 Conclusion

In conclusion, DTAB does not appear to form a plastic crystal, glacial phase, or Frank-Kasper phases. A summary of the broad points just discussed is presented in Table 2.3. X-ray scattering data indicates the development of ordering during a period of isothermal aging. The isothermal aging is not reflected in the  $^2\text{H}$  NMR and IR spectra, suggesting the order is on a larger length scale than is picked up by either technique. SAXS data does not indicate the formation of crystallites or micelles since there is not  $q^{-4}$  dependence. The  $^2\text{H}$  NMR lacking a Pake doublet indicates a high degree of disorder in the decyl tail of the cation. IR spectra demonstrate significant population of both conformers of the  $\text{beti}^-$  anion in the solid phase of DTAB; indicative of conformational disorder.

Table 2.3: Summary of Solid Phases				
Type of Solid	Plastic Crystal	Glacial State	Frank-Kasper Phases	$[\text{N}_{10,111}][\text{beti}]$
Translational Ordering	Yes	No	Yes	Not on a longer length scale than the liquid (XRD)
Rotational/Conformational ordering	No	Crystallites should be ordered, amorphous not.	No	No, $^2\text{H}$ NMR does not show Pake pattern.
Isothermal aging	No	Yes	Yes	X-ray shows evolution while $^2\text{H}$ NMR and IR do not

## Chapter 3: Summary and Conclusions

My initial research concerned NMR measurements of rotational diffusion in 1-butyl-3-methylimidazolium tetrafluoroborate ([Im<sub>41</sub>][BF<sub>4</sub>]) and its mixture with acetonitrile. One study focused on three solutes, dimethylbenzene, cyanomethylbenzene, and dimethylpyridinium hexafluorophosphate in neat [Im<sub>41</sub>][BF<sub>4</sub>]. A second study included rotational and translational diffusion in [Im<sub>41</sub>][BF<sub>4</sub>] mixtures with acetonitrile with benzene as a solute. This work was performed to support computational studies by other group members, and it has already been published. My most recent and independent research involved X-ray scattering, NMR, and IR to characterize the solid phase of trimethyldecylammonium bis(perfluoroethylsulfonyl)imide ([N<sub>10,111</sub>][beti]).

The first rotational diffusion study investigated the effects of molecular size, shape and electrostatics on rotational dynamics in ionic liquids. It could be expected that the magnitude of the solute charge would directly correlate to retardation of the rotational correlation time. However, the distribution of charge within the probe molecule changed the ordering of the local environment. In order from fastest to slowest rotational correlation time was dimethylbenzene, dimethylpyridinium, and cyanomethylbenzene with the slowest rotational correlation times. Thus the rotation of solutes within [Im<sub>41</sub>][BF<sub>4</sub>] depends on the localization of charge and not simply magnitude.

The second study investigated rotational and translational diffusion and provided experimental comparisons for molecular dynamics simulations of mixtures of [Im<sub>41</sub>][BF<sub>4</sub>] with acetonitrile using benzene as a solute. This prototypical system was used to investigate how rotational motion changes with changing composition and viscosity. Rotational diffusion

measurements were found to agree well with simulation, but translational diffusion measurements do not agree for reasons that are still unclear.

The goal of the final study reported here was to determine the nature of the unique solid phase formed by  $[N_{10,111}][\text{beti}]$ . Preliminary XRD and  $^{13}\text{C}$  NMR experiments indicated a superposition of crystalline and amorphous order in the solid phase of  $[N_{10,111}][\text{beti}]$ . Three likely solid phases: plastic crystal, glacial state, and Frank-Kasper phases were used as a framework for subsequent X-ray, NMR, and IR studies. The main foci of experimentation was characterization of the isothermal aging and the length scale of the order in the solid. None of the chosen frameworks provided a full explanation of the data collected, indicating  $[N_{10,111}][\text{beti}]$  does not form a plastic crystal, glacial state, or Frank-Kasper phases in the solid phase. Further analysis of  $[N_{10,111}][\text{beti}]$  is required to more completely determine the nature of its solid phase.

## Appendix: NMR Calibration

### A.1 Temperature Calibration

To verify that our measurements occurred within the extreme narrowing limit,  $T_1$  relaxation times were collected on a 300 MHz instrument as well as the 500 MHz instrument to check the frequency independence of  $T_1$ . Initial comparisons at multiple temperatures did not agree as anticipated and we suspected that the disagreement might be due to errors in the temperature calibrations of the two spectrometers. We therefore devoted some time to calibrating both instruments.

Temperature calibration of NMR spectrometers usually relies upon measuring chemical shift differences in reference materials. Raiford *et al.* published a temperature calibration based on the separation between the methyl and hydroxyl protons at different temperatures<sup>36</sup>. The separation, in ppm, fits to the equation:

$$429.2 - (62.26 \times \Delta\delta) - 13.85 \times (\Delta\delta)^2 \quad (\text{A.1})$$

where  $\Delta\delta$  is the ppm difference between the two peaks of methanol. Raiford *et al.* determined methanol had the best fit over the temperature range 240-310 K. For higher temperatures, ethylene glycol was used similarly. The separation of the peaks fits to the equation:

$$466.0 - 101.64 \times \Delta\delta \quad (\text{A.2})$$

which has a good fit over the temperature range 303-372 K. A later paper by Findeisen *et al.* found that cryoprobes yield extremely broad lines and differences in tuning and matching resulted in differences in the chemical shifts reported<sup>37</sup>. They instead utilized  $^1\text{H}$  spectra of methanol- $\text{d}_4$  and fit the temperature calibration to Eq. A.3.

$$T = -16.7467 \times (\Delta\delta)^2 - 52.5130 \times \Delta\delta + 419.1381 \quad (\text{A.3})$$

Eq. A.3. and methanol-d<sub>4</sub> was used to calibrate the HD 500 MHz instrument.

Figure A.1 shows the results of the calibration of the 300 and 500 MHz instruments. The x-axis reports the temperature reported by the instrument and the y-axis reports the temperatures calculated using the chemical shift difference. The methanol fit (blue) was used to adjust the temperatures below 310 K and the fit of the ethylene glycol data (red) was used to calibrate temperatures above 310 K. The dashed black line indicates the 1:1 between instrument

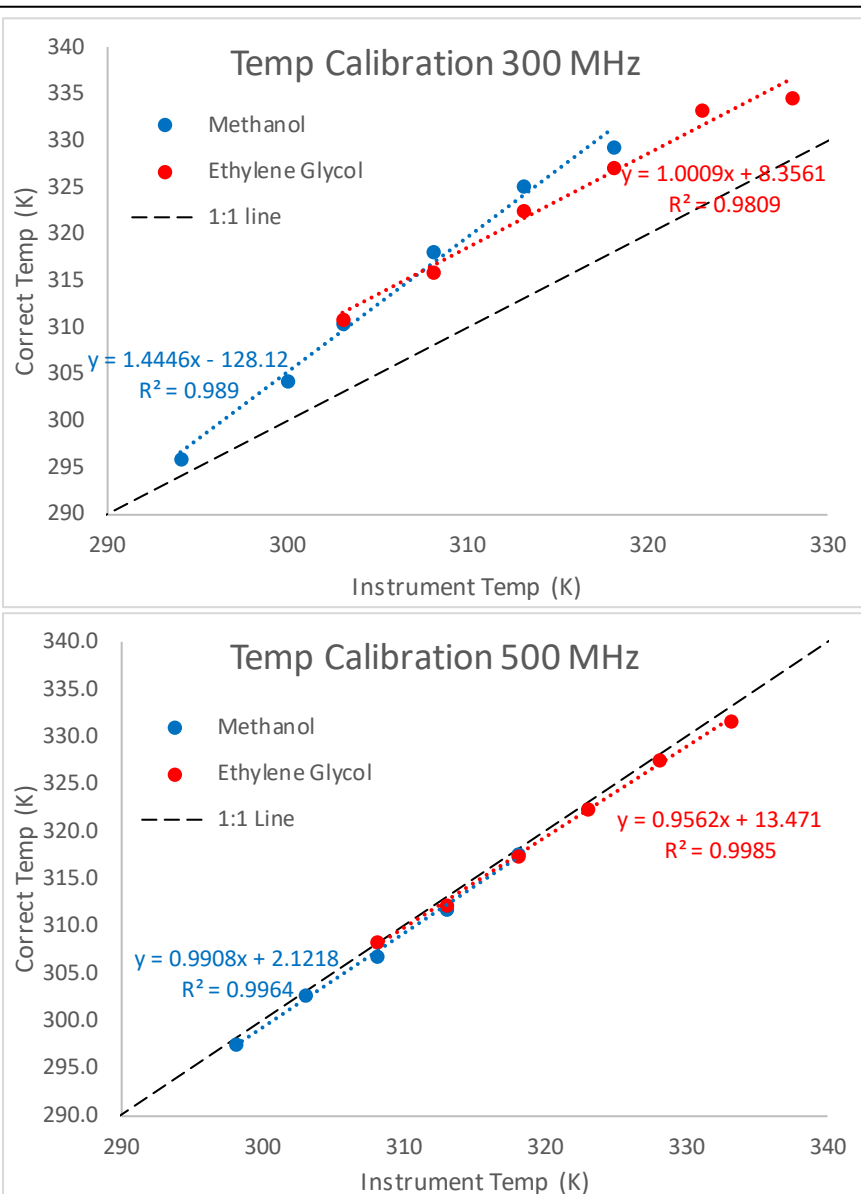


Figure A.1: Calibration curves for 300 MHz (top) and 500 MHz (bottom) NMR instruments. Methanol (blue) and ethylene glycol (orange) temperature data utilize the difference between the proton chemical shifts at different temperatures.

temperature and calculated temperature. The 300 MHz instrument has large discrepancies. Where the instrument reported 318 K, the actual temperature was 329 K, which makes up nearly  $\frac{1}{4}$  the total temperature range observed. The 500 MHz instrument has an internal temperature calibration and so little change was observed between our calculated values and the instrument values.



## A.2 Pulsed Field Gradient Calibration

The PFG experiment is similar in setup to the  $T_1$  experiment. In some ways it is simpler because PFG looks at the proton spectrum and so does not require deuteration

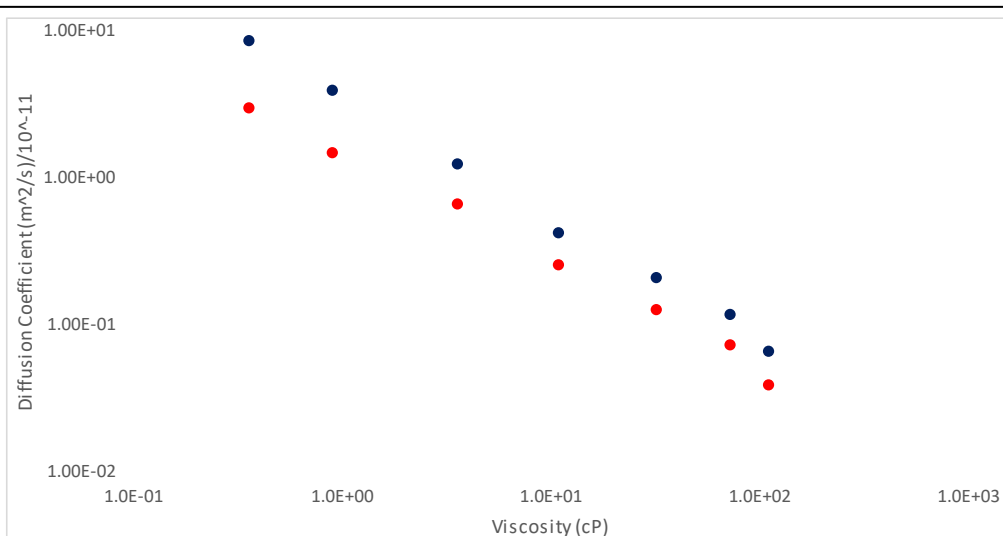
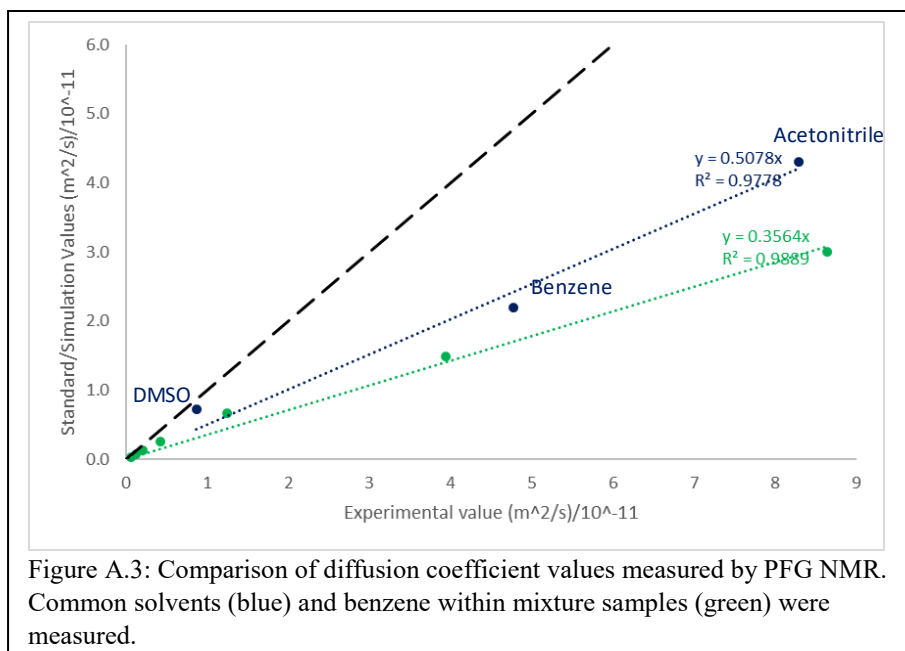


Figure A.2: Comparison of experimental (blue) and simulation (red) diffusion coefficients of benzene in the  $[\text{Im}_{41}][\text{BF}_4]/\text{ACN}$  mixture samples.

of the sample. The main difference is calibration of the gradient pulse. In the  $T_1$  experiment, the delay time is varied to obtain full relaxation. PFG uses a single delay time and varies the gradient strength applied to attenuate the signal. Figure A.2 shows a comparison of the diffusion coefficients of benzene measured experimentally (blue) and calculated in MD simulations (red) within the  $[\text{Im}_{41}][\text{BF}_4]/\text{ACN}$  mixture samples.

The diffusion coefficient for a given PFG experiment utilizes the gradient strength of the NMR instrument used. This gradient strength is a fixed value within the Topspin program that can be manually adjusted. The value for the gradient strength was not calibrated for the PFG experimental results shown in Figure A.2. To determine the accuracy of the gradient strength in Topspin, the experimental diffusion coefficients were compared against simulation values in Figure A.3. In green are the experimentally determined diffusion coefficients for benzene in the  $[\text{Im}_{41}][\text{BF}_4]/\text{ACN}$  mixtures compared against the simulation values from Brian Conway. In blue are conventional solvents compared against literature values for the diffusion coefficients. A 1:1

curve is plotted as a black dashed line. The error between the standard values of the diffusion coefficients and the experimentally measured values appears to be a systematic error. I believe this is caused by a difference between the

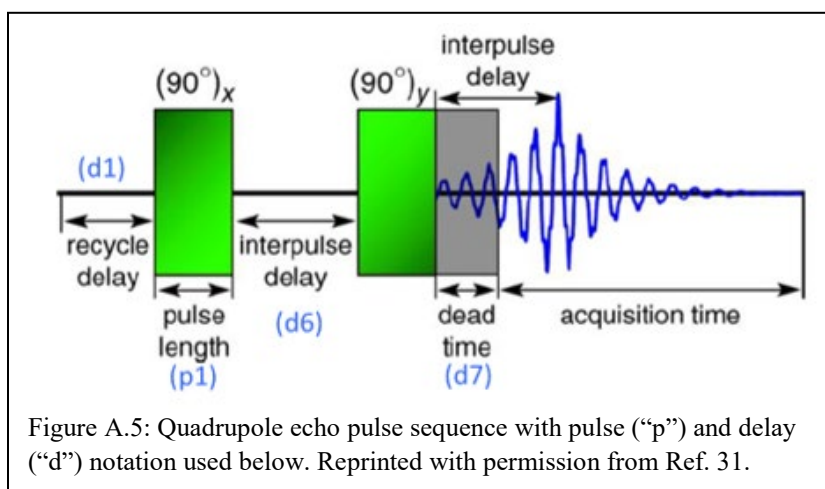


gradient strength reported in the Topspin program and the actual gradient strength delivered to the sample. The error when comparing the experimentally measured diffusion coefficients to the simulated ones has a constant factor as well. I believe this is the same error, but since the sets of data were taken at different times, it is unclear what the difference between reported gradient strength and actual gradient strength was at the time the benzene diffusion data was taken. My recommendation for future PFG experiments is to use an external standard before and after the set of experiments to ensure the correct calibration of the diffusion coefficient of the samples.

### A.3 Solid-state NMR Calibration

The same assumptions that go into setting up a liquid-state NMR experiment do not directly translate to the solid state. The first difference is the solid-state sample needs to be packed into the tube. If the sample is poorly packed into the solid-state tube, the balance will be off, preventing magic-angle spinning (MAS). This was not as important for the  $^2\text{H}$  NMR experiments since they did not spin. It is also important to consider the thermal history of a sample when running MAS experiments. When DTAB was heated above its melting point, the sample would no longer be well-packed for MAS and was off balance. The tube also has a rotor cap to achieve MAS. Certain caps have a smaller effective temperature window because they contact and tend to come off during an experiment. The materials for the caps that we used were Kel-F and Vespel. The Kel-F is meant to be used above 270 K whereas the Vespel caps can go down closer to 230 K.

Calibration of the instrumental parameters was accomplished using external standards of adamantane for  $^1\text{H}$  and  $^{13}\text{C}$  chemical shifts and the shimming parameters. For deuterium lineshape



experiments, hexamethylbenzene- $\text{d}_{18}$  (HMB) and nonadecane- $\text{d}_{40}$  (C19) were used to calibrate the NMR experiments by comparing to literature spectra<sup>31, 33</sup>. Shown in Figure A.5 are the various timings within the solid echo pulse sequence.

Pulse length (p1) was calibrated like the liquid-state experiments. The pulse duration was varied, and I found  $p1 \sim 6.5 \mu\text{s}$  yielded the maximum signal. The acquisition time was a qualitative

adjustment. The only criterion was to avoid truncation of the signal, in order to avoid artifacts in the spectrum. This adjustment was more important for the C<sub>19</sub> and the DTAB compounds, which were more liquid-like near room temperature, thus the FID decayed slowly. All spectra used an acquisition time of at least 8 ms, which seemed long enough for signal to fully decay. The recycle delay (d1), like in the liquid-state, allows the sample to relax to a near equilibrium state before replicate scans are recorded. I used the rule of thumb  $d1 > 5 \times T_1$  to maximize the signal. Kinnun *et al.* used a 0.3 second recycle delay for HMB whereas the nonadecane article used  $d1 = 60$  seconds, due to the rather different values of  $T_1$  for these two solids. However, as long as d1 is much greater than the other times in the pulse sequence, I do not expect d1 to affect the lineshapes obtained.

The two other parameters, the interpulse delay (d6) and the dead time (d7), were more difficult to calibrate. Manipulating these values caused marked changes in the lineshape, but determination of the “correct” value was unclear. Mark and I corresponded with Bruker technicians. The recommendation we received was that additional steps could be taken during the data processing if the d6 or d7 times were not set perfectly. The focus is collecting data beginning at the top of the echo. The interpulse delay sets what time the echo appears, and it is possible to vary d7 to collect from the top of the echo, but it is more reproducible to use left-shifting. For the solid echo pulse sequence, the lineshape is dependent on where data collection starts. If the data collection starts before or after the start of the echo, the signal is distorted. Left shifting simply truncates the data.

Adjusting d6 and d7 to determine the correct lineshape is an iterative process. It involves examining the FID to locate the top of the echo. Hovering the cursor over this point will display an “index number”. This index number is how far to left shift the data using the formula  $(2x-2)$  where x is the index number. Type “nsp” for number of shift points and enter the  $2x-2$  result.

Finally, type “ls” to left shift the data and observe the correction. The unshifted data is present so it is simple to vary the nsp value to determine the best shifting.

## References:

1. Baker, G. A.; Baker, S. N.; Pandey, S.; Bright, F. V., An analytical view of ionic liquids. *Analyst* **2005**, *130* (6), 800-8.
2. Cevasco, G.; Chiappe, C., Are ionic liquids a proper solution to current environmental challenges? *Green Chemistry* **2014**, *16* (5), 2375-2385.
3. MacFarlane, D. R.; Tachikawa, N.; Forsyth, M.; Pringle, J. M.; Howlett, P. C.; Elliott, G. D.; Davis, J. H.; Watanabe, M.; Simon, P.; Angell, C. A., Energy applications of ionic liquids. *Energy & Environmental Science* **2014**, *7* (1), 232-250.
4. Rumble, C. A.; Uitvlugt, C.; Conway, B.; Maroncelli, M., Solute Rotation in Ionic Liquids: Size, Shape, and Electrostatic Effects. *J. Phys. Chem. B* **2017**, *121* (19), 5094-5109.
5. Conway, B.; Uitvlugt, C.; Maroncelli, M., Simulations of 1-Butyl-3-methylimidazolium Tetrafluoroborate + Acetonitrile Mixtures: Force-Field Validation and Frictional Characteristics. *The Journal of Physical Chemistry B* **2018**, *122* (29), 7385-7393.
6. Rumble, C. A.; Kaintz, A.; Yadav, S. K.; Conway, B.; Araque, J. C.; Baker, G. A.; Margulis, C.; Maroncelli, M., Rotational Dynamics in Ionic Liquids from NMR Relaxation Experiments and Simulations: Benzene and 1-Ethyl-3-Methylimidazolium. *J. Phys. Chem. B* **2016**, *120* (35), 9450-67.
7. Levitt, M. H., *Spin Dynamics: Basics of Nuclear Magnetic Resonance*. 2nd ed.; John Wiley & Sons Ltd: West Sussex PO19 8SQ, England, 2008; p 714.
8. Kaintz, A. E.; Maroncelli, M., Translational and rotational diffusion in ionic liquids. p. 1 electronic document (176 pages) Ph.D. Thesis. <https://etda.libraries.psu.edu/paper/17703/>.
9. Jiang, W.; Wang, Y.; Voth, G. A., Molecular dynamics simulation of nanostructural organization in ionic liquid/water mixtures. *J. Phys. Chem. B* **2007**, *111* (18), 4812-8.
10. Liang, M.; Zhang, X. X.; Kaintz, A.; Ernsting, N. P.; Maroncelli, M., Solvation dynamics in a prototypical ionic liquid + dipolar aprotic liquid mixture: 1-butyl-3-methylimidazolium tetrafluoroborate + acetonitrile. *J. Phys. Chem. B* **2014**, *118* (5), 1340-52.
11. Mizuhata, M.; Maekawa, M.; Deki, S., Ordered structure in room temperature molten salts containing aliphatic quaternary ammonium ions. *ECS Transactions* **2007**, *3* (35), 89-95.
12. Apperley, D. C.; Harris, R. K.; Hodgkinson, P., *Solid-State NMR: Basic Principles and Practice*. Momentum Press: 2012.
13. De Graef, M.; McHenry, M. E., *Structure of materials: an introduction to crystallography, diffraction and symmetry*. Cambridge University Press: 2012.
14. MacFarlane, D. R.; Forsyth, M., Plastic Crystal Electrolyte Materials: New Perspectives on Solid State Ionics. *Adv. Mater.* **2001**, *13* (12-13), 957-966.
15. Timmermans, J., Plastic Crystals - a Historical Review. *J. Phys. Chem. Solids* **1961**, *18* (1), 1-8.
16. McGrath, K. J.; Weiss, R. G., NMR Investigation of Molecular Motion in the Neat Solid and Plastic-Crystalline Phases of Cyclohexane. *Langmuir* **1997**, *13* (16), 4474-4479.
17. Zhu, H.; Wang, X.; Vijayaraghava, R.; Zhou, Y.; MacFarlane, D. R.; Forsyth, M., Structure and Ion Dynamics in Imidazolium-Based Protic Organic Ionic Plastic Crystals. *The journal of physical chemistry letters* **2018**, *9* (14), 3904-3909.
18. Makhlooghiazad, F.; Guazzagaloppa, J.; O'Dell, L. A.; Yunis, R.; Basile, A.; Howlett, P. C.; Forsyth, M., The influence of the size and symmetry of cations and anions on the physicochemical behavior of organic ionic plastic crystal electrolytes mixed with sodium salts. *PCCP* **2018**, *20* (7), 4721-4731.

19. Seeber, A. J.; Forsyth, M.; Forsyth, C. M.; Forsyth, S. A.; Annat, G.; MacFarlane, D. R., Conductivity, NMR and crystallographic study of N, N, N, N-tetramethylammonium dicyanamide plastic crystal phases: an archetypal ambient temperature plastic electrolyte material. *PCCP* **2003**, 5 (12), 2692-2698.
20. Jin, L.; Nairn, K. M.; Forsyth, C. M.; Seeber, A. J.; MacFarlane, D. R.; Howlett, P. C.; Forsyth, M.; Pringle, J. M., Structure and transport properties of a plastic crystal ion conductor: diethyl (methyl)(isobutyl) phosphonium hexafluorophosphate. *J. Am. Chem. Soc.* **2012**, 134 (23), 9688-9697.
21. Guinet, Y.; Denicourt, T.; Hedoux, A.; Descamps, M., The contribution of the Raman spectroscopy to the understanding of the polyamorphism situation in triphenyl phosphite. *J. Mol. Struct.* **2003**, 651, 507-517.
22. Faria, L. F.; Matos, J. R.; Ribeiro, M. C., Thermal analysis and Raman spectra of different phases of the ionic liquid butyltrimethylammonium bis(trifluoromethylsulfonyl)imide. *J. Phys. Chem. B* **2012**, 116 (30), 9238-45.
23. Frank, F. t.; Kasper, J., Complex alloy structures regarded as sphere packings. II. Analysis and classification of representative structures. *Acta Crystallogr.* **1959**, 12 (7), 483-499.
24. Kim, S. A.; Jeong, K.-J.; Yethiraj, A.; Mahanthappa, M. K., Low-symmetry sphere packings of simple surfactant micelles induced by ionic sphericity. *Proceedings of the National Academy of Sciences* **2017**, 114 (16), 4072-4077.
25. Lee, S.; Bluemle, M. J.; Bates, F. S., Discovery of a Frank-Kasper  $\sigma$  phase in sphere-forming block copolymer melts. *Science* **2010**, 330 (6002), 349-353.
26. Jin, H.; O'Hare, B.; Dong, J.; Arzhantsev, S.; Baker, G. A.; Wishart, J. F.; Benesi, A. J.; Maroncelli, M., Physical Properties of Ionic Liquids Consisting of the 1-Butyl-3-Methylimidazolium Cation with Various Anions and the Bis(trifluoromethylsulfonyl)imide Anion with Various Cations. *The Journal of Physical Chemistry B* **2008**, 112 (1), 81-92.
27. Murata, K.-i.; Tanaka, H., Microscopic identification of the order parameter governing liquid-liquid transition in a molecular liquid. *Proceedings of the National Academy of Sciences* **2015**, 201501149.
28. Szulzewsky, K.; Schulz, B.; Vollhardt, D., The crystal structure of dodecyltrimethylammoniumbromide. *Cryst. Res. Technol.* **1983**, 18 (8), 1003-1008.
29. Araque, J. C.; Hettige, J. J.; Margulis, C. J., Modern Room Temperature Ionic Liquids, a Simple Guide to Understanding Their Structure and How It May Relate to Dynamics. *The Journal of Physical Chemistry B* **2015**, 119 (40), 12727-12740.
30. Jelinski, L. W., Solid state deuterium NMR studies of polymer chain dynamics. *Annu. Rev. Mater. Sci.* **1985**, 15 (1), 359-377.
31. Kinnun, J. J.; Leftin, A.; Brown, M. F., Solid-State NMR Spectroscopy for the Physical Chemistry Laboratory. *J. Chem. Educ.* **2013**, 90 (1), 123-128.
32. Pake, G. E., Nuclear resonance absorption in hydrated crystals: fine structure of the proton line. *The Journal of chemical physics* **1948**, 16 (4), 327-336.
33. Taylor, M. G.; Kelusky, E. C.; Smith, I. C.; Casal, H. L.; Cameron, D. G., A  $^2\text{H}$  NMR study of the solid-phase behavior of nonadecane. *The Journal of Chemical Physics* **1983**, 78 (8), 5108-5112.
34. Hentschel, D.; Sillescu, H.; Spiess, H., Chain motion in the amorphous regions of polyethylene as revealed by Deuteron magnetic resonance. *Macromolecules* **1981**, 14 (5), 1605-1607.

35. Grondin, J.; Talaga, D.; Lassègues, J.; Johansson, P.; Henderson, W., Spectroscopic and ab initio characterization of the conformational states of the bis (perfluoro-ethanesulfonyl) imide anion (BETI<sup>-</sup>). *Journal of Raman Spectroscopy* **2007**, *38* (1), 53-60.
36. Raiford, D. S.; Fisk, C. L.; Becker, E. D., Calibration of Methanol and Ethylene-Glycol Nuclear Magnetic-Resonance Thermometers. *Anal. Chem.* **1979**, *51* (12), 2050-2051.
37. Findeisen, M.; Brand, T.; Berger, S., A <sup>1</sup>H NMR thermometer suitable for cyroprobes. *Magn. Reson. Chem.* **2007**, *45*, 4.